Accurate steam-water equation of state for two-phase flow LMNC model with phase transition

Stéphane Dellacherie, Gloria Faccanoni, Bérénice Grec, Yohan Penel

Accurate steam-water equation of state for two-phase flow LMNC model with phase transition*

Stéphane Dellacherie[†] Gloria Faccanoni[‡] Bérénice Grec[§¶] Yohan Penel[‖]

Abstract

This paper is dedicated to the design of incomplete equations of state for a two-phase flow with phase transition that are specific to the low Mach number regime. It makes use of the fact that the thermodynamic pressure has small variations in this regime. These equations of state supplement the 2D Lmnc model introduced in previous works.

Our innovative strategy relies on tabulated values and is proven to satisfy crucial thermodynamic requirements such as positivity, monotonicity, continuity. In particular, saturation values are exact. This procedure is assessed by means of analytical steady solutions and comparisons with standard analytical equations of state, and shows a great improvement in accuracy.

Keywords. Thermal-hydraulics; Low Mach number regime; Phase transition; Tabulated equations of state; Thermodynamic consistency; Numerical simulations.

1 Introduction

The present paper follows previous articles and conference proceedings [1–4] devoted to the modelling and the numerical simulation of the coolant fluid in a nuclear reactor of *Pressurised Water Reactor* (PWR) type. We are interested in situations where the Mach number can be considered small (typically of order $\mathcal{O}(10^{-2})$), which is equivalent to assuming that the material velocity is much smaller than the speed of sound. It is in particular the case in nominal and some incidental situations, and this makes this approach relevant as a preliminary study for safety evaluations.

The low Mach number assumption strongly influences both theoretical and numerical approaches in the modelling process. It has been proven in numerous works that issues may occur in a compressible framework when the Mach number $\mathcal{M}$ is quite small (see for instance [5,6] and references therein). The pressure variable is mainly held responsible for such instabilities, due to the singularity of the pressure terms with respect to $\mathcal{M}$, and due to the propagation of initial perturbations. Let us recall some results:

- First, solutions of a compressible model are expected to formally converge to incompressible solutions when $\mathcal{M}$ goes to 0. However, this only happens under suitable conditions on inputs to the model: the initial conditions (of correct orders of magnitude, *i.e.*well-prepared), the domain of the flow and the equation of state modelling water properties (see for instance [7–11] and references therein).
- Second, even with well-prepared initial conditions, classic numerical schemes may lead to inaccurate solutions, *i.e.* that are not consistent with the compressible model and exhibit spurious waves [6, 12]. It has been proven that the numerical schemes do not have steady states that are consistent approximations of the steady states of the model [5].
- Third, in addition to accuracy issues, efficiency of numerical methods is also pointed out. Indeed, low Mach number flows correspond to cases where time scales induced by the speed of sound and by the flow velocity are quite different. An explicit stability condition would take the speed of sound into account and over-constrain the computations. In contrast, an implicit scheme would fail to reproduce fast physical phenomena.

*This work was partially funded by the CNRS project call NEEDS (nuclear, energy, environment, waste and society) for which the LMNC/LMNC2 projects were selected in 2014–2017.

[†]Hydro-Québec, TransÉnergie, 75 boulevard René-Lévesque Ouest, Montréal (Qc), H2Z 1A4, Canada – dellacherie.stephane@hydro.qc.ca

[‡]Université de Toulon – IMATH, EA 2134, avenue de l'Université, 83957 La Garde, France – faccanoni@univ-tln.fr

[§]Corresponding author

[¶]MAP5 UMR CNRS 8145 - Université Paris Descartes - Sorbonne Paris Cité, 45 rue des Saints Pères, 75270 Paris Cedex 6, France – berenice.grec@parisdescartes.fr

[‖]CEREMA–Inria (team ANGE) and Sorbonne Universités, UPMC Univ. Paris 06, LJLL UMR CNRS 7598, 75005 Paris, France – yohan.penel@cerema.fr

For all these reasons, three main strategies have been considered in the literature:

① From the numerical point of view, splitting strategies have been introduced to simulate compressible flows. They rely on a decomposition of the compressible operators between non-stiff terms (handled explicitly) and stiff terms (handled implicitly). Stiff terms are classically the pressure [13–15] or more generally acoustic terms [16–18]. Other methods are based on a Lagrange-projection [19] or on a Hodge decomposition [20]. In [21, 22], preconditioning techniques are used to deal with diffusion terms.

② The inaccuracy of classic schemes has been analysed by means of asymptotic expansions with respect to the Mach number. This resulted in modified versions of the compressible schemes to treat the low Mach regime [23, 24]. In particular, some corrected Godunov-type schemes have been derived so that the kernel of the continuous operator matches with its discrete counterpart.

③ Another strategy consists in deriving models of reduced complexity which are specific to the low Mach number regime [3, 25–28]. Asymptotic expansions with respect to the Mach number are applied to the compressible model, and this leads to a hierarchy of intermediate (simpler) models between compressible and incompressible systems. However, applications of those simplified models are restricted to cases where acoustics can be neglected, since the truncation of the asymptotic expansion amounts to filtering out acoustic waves.

The present paper is based on Approach ③, since acoustics phenomena are not predominant in the context we are investigating. Models derived in this way have several advantages from both theoretical and numerical points of view. First, their mathematical structure is much simpler than compressible systems. For the Euler equations, the hyperbolic operator becomes a mixed hyperbolic-elliptic operator that transcribes the low Mach number assumption. It comprises a divergence constraint whose source term is not zero (as it would be in the incompressible limit). Second, unlike incompressible models, low Mach number systems account for large heat transfer (through variations of the density). Third, the asymptotic expansion leads to a decoupling of the pressure field into a *dynamic* pressure $\mathcal{P}$ appearing in the momentum equation and a reference *thermodynamic* pressure p_* – involved in the equation of state –, which turns out to be independent from the space variable. The global pressure is recovered by summing the two fields $p_* + \mathcal{M}^2\mathcal{P}$: this means that when the Mach number $\mathcal{M}$ is small, the pressure is constant equal to p_* up to small variations of order $\mathcal{O}(\mathcal{M}^2)$.

The latter characteristic is crucial and has major consequences, of which we are making use in this paper:

- First, it enables the computation of explicit analytical solutions in the 1D case [2, 29]n which provides reliable tools to assess compressible solvers in the low Mach regime.
- Second, it leads to simple robust and efficient numerical schemes, since it turns the standard stability condition for explicit schemes (where acoustics is involved) into a purely convective stability condition. Time steps can thus be chosen to be larger, and the computational cost significantly decreases.
- Third, the fact that the reference thermodynamic pressure can be considered constant in space allows a lower number of evaluations of the equation of state (only once per time iteration) which also reduces the computational cost. The latter consequence is the key-point of the paper.

Most nuclear thermal-hydraulics codes (such as Cathare, Flica4, Thyc, Relap5, Trace [30–35]) are based on the resolution of the compressible Navier-Stokes system. On the contrary, here we propose to work on a simplified model, obtained by filtering out the acoustic waves in such a compressible system. This approach dedicated to the low Mach number regime is complementary to the traditional studies, potentially richer but too complex for a similar analysis. On the one hand, it provides new theoretical and numerical information useful for understanding thermal-hydraulics in the low Mach number regime, especially for innovative concepts with high power density. On the other hand, it can serve as a support for compressible industrial codes to assess them in the low Mach number regime, a regime that is mostly encountered in nuclear thermal-hydraulics, and whose approximation by a compressible numerical scheme can be tricky.

The model investigated in the present paper is named Lmnc for *Low Mach Nuclear Core* model and was designed in [3] for monophasic flows. It is derived from the Navier-Stokes equations in an open bounded domain with a heating source term. Only terms of order 0 are kept in the asymptotic expansion with respect to the Mach number.

In addition to the PDE system, we want to describe water properties thanks to thermodynamics. Classically, PDEs are supplemented with an equation of state (EOS), which is a relation between pressure, density and entropy variables. This relation is expected to transcribe the behaviour of water over a specific range of physical conditions (temperature and pressure). Analytical EOS have been proposed in the literature such as the *ideal gas* law or the *stiffened gas* (SG) law [36, 37]. They have the advantage of a simple formulation leading to explicit computations. In particular, the SG law corresponds to a rational function, involving five parameters to be tuned depending on the range of temperature

under investigation. However, it turns out that any tuning provides inaccurate results for the values relevant in our context, namely for a pressure equal to 15.5 MPa and for high temperatures close to saturation. A similar 6-parameter law (NASG) has been recently designed [38] to cover an extended range of temperature, but the inaccuracy close to saturation still remains. The SG law was mainly used in previous works [1, 2, 4], in order to take advantage of its simple formulation leading to explicit solutions in dimension 1. Analytical laws such as SG and NASG are academic tools which are quite useful to assess models and numerical strategies, but they are known to be restricted to simple cases and could be quite inaccurate as we shall show in this paper: the SG law yields a too late vaporisation that can have dramatic consequences in terms of safety. Hence, to provide more reliable results in particular for safety evaluations, another strategy is necessary for defining equations of state in the range of temperature of interest.

Physical values of main thermodynamic variables are measured over a wide range of pressure/temperature values for water and available for researchers in [39]. A strategy thus consists in constructing fitting polynomials for each physical variable involved in the model which match tabulated data. It would be an expensive computation in a compressible framework since an equation of state depends on two variables [40–42]. But in the low Mach number regime, low Mach number models exhibit a constant thermodynamic pressure which makes the equation of state a function of a single variable (which is not the temperature as in classic works but the enthalpy for reasons explained below). Even if the resulting equation of state has a more complex expression than the SG/NASG laws, it is expected to provide more accurate results in the physical context we are interested in. To this end, fitting polynomials should be very carefully designed [43] to satisfy basic thermodynamic requirements (positivity, monotonicity, ...). We present in this paper an innovative procedure to construct such relevant EOS for pure phases (liquid and vapour) at low Mach numbers.

The challenge is then more tricky when phase transition occurs. In addition to the design of accurate specific equations of state for water and steam, one has to model equilibria across phase transition and saturation phenomena. In the present work, we consider mechanical and thermodynamic equilibria, which amounts to assuming that phases move at the same velocity, and that vaporisation, condensation and heat transfer processes are instantaneous. This is why the Lmnc model is a system with 3 equations and a single velocity field. It can be seen as the zero Mach limit of the HEM model [44] with source terms. Other equilibria can also be considered and would lead to 4- to 7-equation systems.

Under these equilibrium assumptions, water appears under liquid and vapour phases but also as a mixture of the two. Mixture must thus be modelled through the evolution of thermodynamic and mechanical variables. In particular, temperature is constant within the mixture phase. As the differential model must account for the three phases, temperature cannot be chosen as a main variable. This is why the unknown variables involved in the Lmnc model are the enthalpy, the velocity and the dynamic pressure. While complete equations of state are functions of two variables, EOS for low Mach number models are functions of the enthalpy only[1]. For SG or NASG EOS, the saturation is determined by the equality of Gibbs potentials, which may result in inaccurate values at saturation. Figure 1 shows the physical irrelevance of these equations of state. The temperature at saturation for these EOS is larger than the critical temperature at $p = 15.5$ MPa.

The strength of the procedure described in this work is that analytic equations of state are derived from tabulated values and satisfy exactly the saturation. It takes advantage of the fact that the thermodynamic pressure is constant, which enables us to guarantee crucial properties for the well-posedness of the model as well as for the physical relevance of its solutions. Naively, density and temperature could be fitted as functions of enthalpy and then the compressibility coefficient (2) and the heat capacity would be deduced by differentiation. That would raise some consistency and stability issues. By means of thermodynamic relations (see Proposition 3.1), it is possible to do this in reverse: fitting[2] the compressibility coefficient and then integrating to deduce the density. This turns out to be a decisive procedure as it ensures positivity, monotonicity and continuity of the density. Moreover, saturation values exactly match with tabulated ones (Proposition 3.2). The same procedure can be applied independently to the temperature, which is deduced from the isobaric heat capacity with the same mathematical properties. Coefficients of the tabulated equation of state are only computed once (as for SG/NASG laws) as a pre-processing and hold for all iterations. Such an incomplete equation of state is obviously restricted to constant pressure regimes but in the present context, it is a very efficient and stable method to incorporate water physics in the Lmnc model.

The paper is organised as follows. We first present in Section 2 the Lmnc model, which consists of 3 equations involving velocity, enthalpy and dynamic pressure. We mention that viscosity and thermal conductivity are taken into account. Boundary conditions are also specified. The core of the paper is detailed in Section 3: we briefly recall the modelling of mixture (see also [2]) and the expression of the *Stiffened Gas* and *Noble-Abel – Stiffened Gas* laws. We then explain the construction of the dedicated equations of state in pure phases based on the fitting of tabulated values [39]. This amounts to specifying the dependency of all thermodynamic and physical variables with respect to

[1] The reader is reminded that the second variable – the thermodynamic pressure – is constant in this study.

[2] The choice of the fitting procedure is left to the reader. The least square method applied in the present work is not exclusive at all.

the enthalpy. Two strategies are investigated to fit the compressibility coefficient β and the isobaric heat capacity c_p:[3] NIST-p which corresponds to high order polynomial-fitting and NIST-0 which is a phasewise constant approximation. We state the crucial properties satisfied by the corresponding equations of state. In Section 4, we provide mathematical assumptions on data and on the smoothness of solutions (jump conditions across phase transition), and we compare the accuracy of the aforementioned equations of state upon an analytical steady solution. Section 5 is dedicated to numerical simulations to compare the equations of state on a stiff test case, and highlight the influence of the thermal conductivity and of the gravity field.

2 Low Mach two-phase flow model with phase transition and thermal diffusion

2.1 Equations

Fluid flows are often described by the Navier-Stokes equations. When the flow regime is such that the Mach number is small (typically, $\mathcal{M} = \mathcal{O}(10^{-2})$), they can be replaced by simplified models like the Lmnc model derived in [3]. The latter system is mainly investigated under its non-conservative formulation [2, 4]

$$\begin{cases} \nabla\cdot\boldsymbol{u} = \dfrac{\beta(h,p_*)}{p_*}\left[\nabla\cdot\big(\Lambda(h,p_*)\nabla h\big) + \Phi\right], & \text{(1a)} \\ \varrho(h,p_*)\times\left[\partial_t h + \boldsymbol{u}\cdot\nabla h\right] = \nabla\cdot\big(\Lambda(h,p_*)\nabla h\big) + \Phi, \qquad (t,\boldsymbol{x})\in\mathbb{R}^+\times\Omega^d, & \text{(1b)} \\ \varrho(h,p_*)\times\left[\partial_t\boldsymbol{u} + (\boldsymbol{u}\cdot\nabla)\boldsymbol{u}\right] - \nabla\cdot\sigma(\boldsymbol{u}) + \nabla\mathcal{P} = \varrho(h,p_*)\boldsymbol{g}, & \text{(1c)} \end{cases}$$

for some bounded domain[4] $\Omega^d\subset\mathbb{R}^d$, $d\in\{1,2\}$. The unknowns involved in this model are the velocity $\boldsymbol{u}$, the enthalpy h and the dynamic pressure $\mathcal{P}$. The data are the constant[5] thermodynamic pressure p_*, the power density $\Phi(t,\boldsymbol{x})$, which models the heating of the coolant fluid due to the fission reactions in the nuclear core, and the constant gravity field $\boldsymbol{g}$. To close the model, we have to provide the expression of the density $\varrho = \varrho(h,p_*)$ and the compressibility coefficient $\beta(h,p_*)$ – *i.e.* specify the equation of state, see § 3.1 –, the viscous stress tensor $\sigma(\boldsymbol{u})$ – see § 3.2 – and the coefficient $\Lambda = \Lambda(h,p_*)$ which is related to thermal conduction effects – see § 3.3. The present article is dedicated to the modelling of these terms which characterise properties of water through equations of state and physical laws when phase transition is taken into account.

More precisely, the compressibility coefficient is the key variable in this work, and is originally defined by

$$\beta(h,p_*) \overset{\text{def}}{=} -\frac{p_*}{\varrho(h,p_*)^2}\cdot\left.\frac{\partial\varrho}{\partial h}\right|_p(h,p_*). \tag{2}$$

Another expression of β is designed in Proposition 3.1 which turns out to be crucial for the study. Notice that the term *compressibility* has been originally chosen to remind its relation with the compressibility of the flow through the divergence constraint. It is also referred to as the thermal expansion coefficient in previous works. Both denominations are imprecise as they are also respectively used in the literature to refer to $\beta_T \overset{\text{def}}{=} -\frac{1}{\tau}\left.\frac{\partial\tau}{\partial p}\right|_T$ or to $\beta_p \overset{\text{def}}{=} \frac{1}{\tau}\left.\frac{\partial\tau}{\partial T}\right|_p$, where $\tau = 1/\varrho$ (see for instance [45–47]). We keep the denomination *compressibility coefficient* in what follows, keeping in mind its relation with other thermodynamic coefficients.[6]

As for viscous effects, they include the classic internal friction in the fluid, as well as the friction on the fluid due to technological devices in the nuclear core (*e.g.* the friction on the fluid due to the fuel rods):

$$\sigma(\boldsymbol{u}) = \mu(h,p_*)\times\left(\nabla\boldsymbol{u} + \nabla^T\boldsymbol{u}\right) + \eta(h,p_*)\times(\nabla\cdot\boldsymbol{u})\,\mathcal{I}_d.$$

The very expression of the viscous term is not important in the 1D framework as (1c) decouples from the other equations [2]. The computation of $\mathcal{P}$ is then only a postprocessing. This is no more the case in higher dimensions where the latter equation is a real part of the coupled system.

When a monophasic flow is considered, System (1) is then coupled to an equation of state and to physical laws dedicated to a pure phase. To go further by taking into account phase transition, it is necessary to specify the

[3] Unlike the SG/NASG laws where β and c_p are fully determined by the parameters of the laws, in the NIST strategy, they are computed independently from each other.

[4] In 1D, $\Omega^1 = [0, L_y]$, $\boldsymbol{x} = y$ and $\boldsymbol{u} = v$, whereas in 2D $\Omega^2 = [0, L_x]\times[0, L_y]$, $\boldsymbol{x} = (x, y)$ and $\boldsymbol{u} = (u, v)$. We do not study the 3D case in this paper but the extension is straightforward.

[5] In the low Mach approximation, the thermodynamic pressure p_* does not depend on space but in general it can be considered a function of time [1, 26]. We focus here on applications where it can be assumed to be constant.

[6] In particular, we have $\beta = \frac{p\tau\beta_p}{c_p}$.

equilibria at stake between phases. In the present case, we assume that phases are in thermodynamic and mechanic equilibria which induces the equality of temperatures, pressures, Gibbs potentials and velocities. As a consequence, this model has a single velocity for all phases under which water appears. As we shall see below, System (1) has a simpler structure than the Navier-Stokes equations which makes it easier to treat phase transition.

We must also emphasise that System (1) is characterised by two pressure fields, which is classic in low Mach number approaches: the *thermodynamic pressure* p_* is involved in the equation of state while the *dynamic pressure* $\mathcal{P}$ appears in Equation (1c). This pressure decomposition results from an asymptotic expansion with respect to the Mach number which induces the filtering out of the acoustic waves which are not involved anymore in System (1).

2.2 Boundary conditions

Boundary conditions are specified in 2D but adapt directly to 1D (see Figure 2). We denote by $\boldsymbol{n}$ the unit outer normal vector to each boundary, and by $\boldsymbol{\tau}$ a unit tangential vector so that $(\boldsymbol{n}, \boldsymbol{\tau})$ is a direct basis.

- The fluid is injected at the bottom $y = 0$ of the core at a given density ϱ_e and at a given vertical flow rate D_e:

$$\varrho\big(h(t,x,0), p_*\big) = \varrho_e(t,x), \tag{3a}$$
$$(\varrho \boldsymbol{u})(t,x,0) = \big(0, D_e(t,x)\big). \tag{3b}$$

  The entrance enthalpy $h_e(t,x)$ is implicitly defined by the equation $\varrho(h_e, p_*) = \varrho_e$. The vertical entrance velocity $v_e(t,x)$ applied at $y = 0$ is deduced from the relation $v_e(t,x) = D_e(t,x)/\varrho_e(t,x)$.

- As for the temperature, we impose adiabatic conditions on all boundaries, except at the entry:

$$\Lambda(h,p_*)\nabla h \cdot \boldsymbol{n}(t,0,y) = \Lambda(h,p_*)\nabla h \cdot \boldsymbol{n}(t,L_x,y) = 0, \qquad \text{[lateral walls]}$$
$$\Lambda(h,p_*)\nabla h \cdot \boldsymbol{n}(t,x,L_y) = 0. \qquad \text{[top]}$$

- On the lateral walls we consider Robin conditions on the velocity:

$$(\boldsymbol{u}\cdot\boldsymbol{n})(t,0,y) = (\boldsymbol{u}\cdot\boldsymbol{n})(t,L_x,y) = 0,$$
$$\sigma(\boldsymbol{u})\boldsymbol{n}\cdot\boldsymbol{\tau}(t,0,y) = \sigma(\boldsymbol{u})\boldsymbol{n}\cdot\boldsymbol{\tau}(t,L_x,y) = 0.$$

- Finally, at the top of the core, we consider a free outflow

$$\big[\sigma(\boldsymbol{u})\boldsymbol{n} - \mathcal{P}\boldsymbol{n}\big](t,x,L_y) = \boldsymbol{0}. \tag{3c}$$

  Let us mention that it comes from the following boundary condition for the "parent model" (Navier-Stokes for a compressible fluid)[7]

$$\big[\sigma(\boldsymbol{u})\boldsymbol{n} - p\boldsymbol{n}\big](t,x,L_y) = -p_*\boldsymbol{n}.$$

Remark 2.1. *In a previous 1D work [2], we considered slightly different boundary conditions. First, (3a) replaces $h(t,x,0) = h_e(t,x)$ for a given h_e in [2]. Imposing ϱ_e or h_e is not completely equivalent since it depends on the choice of the equation of state $\varrho(\cdot, p_*)$. In particular, it implies that steady states for distinct EOS are different (see Proposition 4.1 and Figure 7(a)). Nevertheless, for any accurate EOS, both choices lead to similar results.*

Second, (3c) replaces $\mathcal{P}(t,x,L_y) = 0$ in [2]. They are nothing but the same when no viscous effects are taken into account ($\mu \equiv \eta \equiv 0$). However, in the viscous case, they are actually different. In the 1D case, we can exhibit analytical steady and unsteady solutions and the resultats are of the same order due to the values of viscosity. In 2D, (3c) is necessary for theoretical reasons (see the weak formulation in § 5.2), as well as for physical reasons since $\mathcal{P} = 0$ is hard to impose.

3 Accurate steam-water closures for the two-phase flow Lmnc model with phase transition

In this section, we present different strategies to close the model by means of equations of state (EOS) and physical laws. These relations between thermodynamic and physical variables are expected to accurately transcribe properties of water over a range of enthalpy values (h_{min}, h_{max}) – to be specified –, so that we can reproduce the behaviour

[7] The physical pressure field p is recovered from pressure in the low Mach number model by $p = p_* + \mathcal{P}$. Thus $\mathcal{P} = \mathcal{O}(\mathcal{M}^2)$ is a perturbation around the mean value p_*.

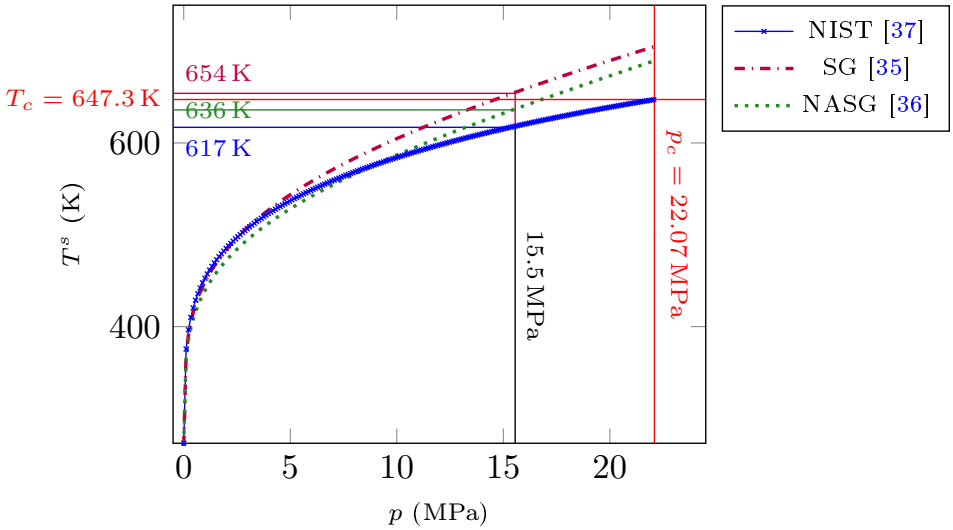

Figure 1: Temperature at saturation as a function of the pressure. Notice that at $p = 155\,\mathrm{bar}$, $T^s_{\mathrm{SG}} > T_c > T^s_{\mathrm{NASG}} > T^s_{\mathrm{NIST}}$.

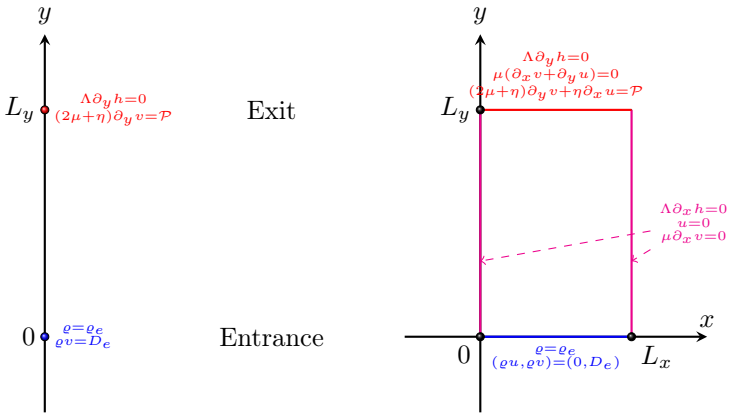

(a) Domain Ω^1 (b) Domain Ω^2

Figure 2: Domain Ω^d, $d \in \{1, 2\}$ and boundary conditions

of the flow in a realistic way. On the one hand, we mention that the narrower the interval, the more accurate the modelling. On the other hand, we have to take an interval large enough to handle incidental values close to phase transition (hence close to the enthalpy at saturation in liquid water and vapour phase).

An EOS is related to thermodynamic properties of a fluid and consists of an algebraic/differential relation between thermodynamic variables. An EOS must satisfy thermodynamic constraints: the term inside the square root in the definition of the speed of sound – see (28) in Appendix C – must be positive; the density must be a monotone-decreasing function of the enthalpy. The other issue is to derive an EOS that models not only pure liquid and vapour phases of water but also the transition from one phase to another in a relevant and accurate way. A badly calibrated EOS may dramatically modify the temperature at saturation in the fluid and cause unphysical phase transition from liquid to vapour.

Since the fluid is considered a continuum (see *e.g.* [48, 49] for a review of multiphase flow modelling), we consider here that water can appear under liquid phase (referred to by the index $\kappa = \ell$), vapour phase ($\kappa = g$), or a mixture of liquid and vapour ($\kappa = m$). The overall problem could be treated by means of distinct models for each phase supplemented with transmission conditions when phase transition occurs as it is the case for immiscible fluids. Our model relies on the assumption of local kinematic and thermodynamic equilibria between phases. This means that phases are assumed to evolve at the same velocity, and that vaporisation, condensation and heat transfer processes are assumed to be instantaneous. As a result, we rather model the two-phase flow by means of a single system of PDEs (with a single velocity field), governing physical variables no matter what the phase they are related to. This process holds provided the EOS has a wide domain of validity including phase transition. For more details on the construction of these EOS and their applications to CFD for compressible fluid flows, see for instance [44, 50–53].

Variables to be defined as functions of (h, p_*) are ϱ, β, Λ, μ and η involved in (1) as well as c_p and T for postprocessing. In classic thermodynamics, two variables are sufficient to represent a thermodynamic state for a pure single-phase fluid through the EOS. In the literature, there exist numerous EOS specific to each fluid under investigation. The case of liquid-vapour phase transitions is schematically depicted on Figure 3 and represented by means of experimental data extracted from [39] on Figure 4. When phase transition is taken into account, a mixture zone appears where the two phases co-exist: it is called the *saturation zone* (Figs. 3a and 4a). This region is bounded by two saturation curves connected at the critical point $(1/\varrho_c, p_c)$ which also belongs to the critical isotherm $T = T_c$. Since phase transition appears at constant pressure and temperature, the physical isotherm is horizontal.

Once an EOS is provided for both liquid and vapour phases, the equality of Gibbs potentials leads to the definition of the temperature at saturation and then to enthalpies at saturation $h_\ell^s(p_*)$ and $h_g^s(p_*)$ [36, 46]. To model phase transition, we introduce a phasewise decomposition for any variable $\zeta \in \{\varrho, \beta, T, \Lambda, c_p, \mu, \eta\}$:

$$\zeta(h, p_*) = \begin{cases} \zeta_\ell(h, p_*), & \text{if } h \leq h_\ell^s(p_*), \\ \zeta_m(h, p_*), & \text{if } h_\ell^s(p_*) < h < h_g^s(p_*), \\ \zeta_g(h, p_*), & \text{if } h \geq h_g^s(p_*). \end{cases} \tag{4}$$

From now on, we shall ignore the dependency with respect to p_* for thermodynamic variables as the thermodynamic pressure is constant throughout this study.

To construct the global EOS, we aim at constructing explicit functions $h \mapsto \widetilde{\zeta}_\kappa(h)$, $\kappa \in \{\ell, g\}$, approximating $h \mapsto \zeta_\kappa(h, p_*)$ so that each pure phase has its own thermodynamics described in an accurate way. Then, the modelling of the mixture $\widetilde{\zeta}_m$ is carried out by means of an analytical formula based on thermodynamic principles [2, § 3.2].

Notations. *In what follows, we shall adopt the following notations:*

- ζ_κ *refers to the generic thermodynamic variable in phase* κ*;*
- $\widetilde{\zeta}_\kappa$ *is a polynomial-fitting approximating* ζ_κ*: the core of this paper is to present different approaches to design such functions;*
- $(\widehat{\zeta}_\kappa)_i$ *are the tabulated values for* ζ_κ *extracted from the NIST tables [39];*
- *In case when* ζ_κ *can be considered constant, the corresponding constant value is denoted by* $\overline{\zeta}_\kappa$*.*

A natural approach is to try to design a complete EOS in which $T(h, p_*)$ and $\varrho(h, p_*)$ are constructed in the first place, and then $\beta(h, p_*)$ and $c_p(h, p_*)$ are deduced from (2) and (26). However, as we shall see in the following, for stability and consistency reasons we prefer constructing an incomplete EOS based on $\beta(h, p_*)$.

In this work, we detail several strategies to derive an EOS for pure phases. We shall consider analytical EOS such as ❶ the *Stiffened Gas* (SG) law (see for instance [36, 37]) or ❷ the *Noble-Abel – Stiffened Gas* (NASG) law [38]. We also investigated strategies based on experimental measurements gathered in tables [39, 40], which will be referred

to as ❸ NIST-p for high-degree polynomial-fitting $h \mapsto \widetilde{\zeta}_\kappa(h)$ and ❹ NIST-0 for constant approximations $\overline{\zeta}_\kappa$. We underline that this is a strength of the low Mach number approach: in a compressible framework, one would have to derive a function $(h,p) \mapsto \widetilde{\zeta}_\kappa(h,p)$ that fits a surface of tabulated values, whereas in the low Mach framework, the procedure reduces to fitting a curve, since the polynomial only depends on h ($p \equiv p_*$ here).

Since these fitting functions cannot model the behaviour of water for all values of h, we focus on a restricted interval of values, prescribed in the following Hypothesis.

Hypothesis 3.1. *Functions ϱ, β, T, Λ, c_p, μ and η are defined over the interval (h_{min}, h_{max}) where h_{min} and h_{max} satisfy:*

1. *there exists a unique $h_e \in (h_{min}, h_{max})$ satisfying $\varrho(h_e, p_*) = \varrho_e$ in order to apply the boundary condition (3a);*
2. $h_{min} > h_\ell^s - \dfrac{p_*}{\varrho_\ell^s \max\limits_{h\in[h_{min},h_\ell^s]} \beta(h,p_*)}$ *and* $h_{min} > h_\ell^s - \dfrac{T^s}{\max\limits_{h\in[h_{min},h_\ell^s]} \dfrac{1}{c_p(h,p_*)}}$.

Hypothesis 3.1-2. is necessary in order to ensure the positivity of ϱ over $[h_{min}, h_\ell^s]$ for the construction (12) of $1/\varrho$ and the positivity of T over $[h_{min}, h_\ell^s]$ for the construction (18).

3.1 Compressibility coefficient and density

Let us now detail how we construct the global fitting function $\widetilde{\beta}$ defined phasewise as in (4) *via* the EOS $\widetilde{\beta}_\kappa$ in each phase $\kappa \in \{\ell, m, g\}$.

3.1.1 Compressibility coefficient and density in the mixture phase

As detailed in [2, § 3.2], the compressibility coefficient in the mixture is phasewise constant and given by

$$\overline{\beta}_m \stackrel{\text{def}}{=} p_* \frac{1/\varrho_g^s - 1/\varrho_\ell^s}{h_g^s - h_\ell^s}. \tag{5a}$$

The derivation is much simpler than in the fully compressible case [54].

Let us mention that the expression of $\overline{\beta}_m$ does not depend on the EOS in pure phases but only on values at saturation, which may differ from one strategy to another (see Table 4). As for the density, it reads

$$\varrho_m(h) \stackrel{\text{def}}{=} \frac{\varrho_g^s \varrho_\ell^s (h_g^s - h_\ell^s)}{\varrho_g^s h_g^s - \varrho_\ell^s h_\ell^s - (\varrho_g^s - \varrho_\ell^s) h}. \tag{5b}$$

Given the two latter definitions, we can write

$$\frac{1}{\varrho_m(h)} = \frac{\overline{\beta}_m}{p_*}(h - \overline{q}_m)$$

where

$$\overline{q}_m \stackrel{\text{def}}{=} \frac{\varrho_g^s h_g^s - \varrho_\ell^s h_\ell^s}{\varrho_g^s - \varrho_\ell^s}. \tag{5c}$$

Hence this process which results from thermodynamic arguments makes the mixture EOS look like the *Stiffened Gas* law (7).

3.1.2 Compressibility coefficient and density in pure phases

Let us then present the construction of $\widetilde{\beta}_\ell$ and $\widetilde{\beta}_g$, as well as $\widetilde{\varrho}_\ell$ and $\widetilde{\varrho}_g$, for the different approaches we consider.

❶-❷ **SG-NASG**: The *Stiffened Gas* (SG) law and the *Noble-Abel Stiffened Gas* (NASG) law result from the same construction process, namely a complete equation of state (after Menikoff and Plohr [36]) which is a smooth relation between the specific entropy $\mathcal{S}$, the specific volume $\tau \stackrel{\text{def}}{=} 1/\varrho$ and the specific energy ε

$$(\tau, \varepsilon) \mapsto \mathcal{S}(\tau, \varepsilon) = \overline{c}_v \left[\ln\left(\varepsilon - \overline{Q} - \overline{\pi}(\tau - \overline{b})\right) + (\overline{\gamma} - 1)\ln(\tau - \overline{b}) \right] + \overline{\mathcal{S}}_0, \tag{6}$$

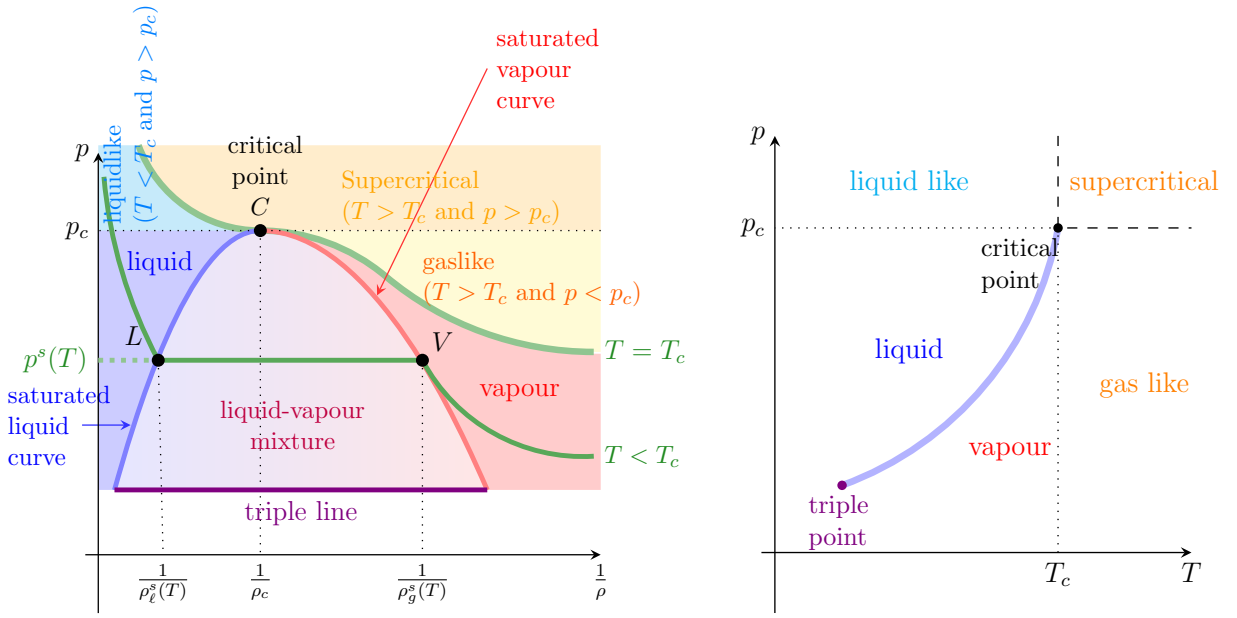

(a) Scheme of isotherms in the $(1/\varrho, p)$ plane

(b) Scheme of coexistence curve in the (T, p) plane

Figure 3: Schematic saturation and coexistence curves.

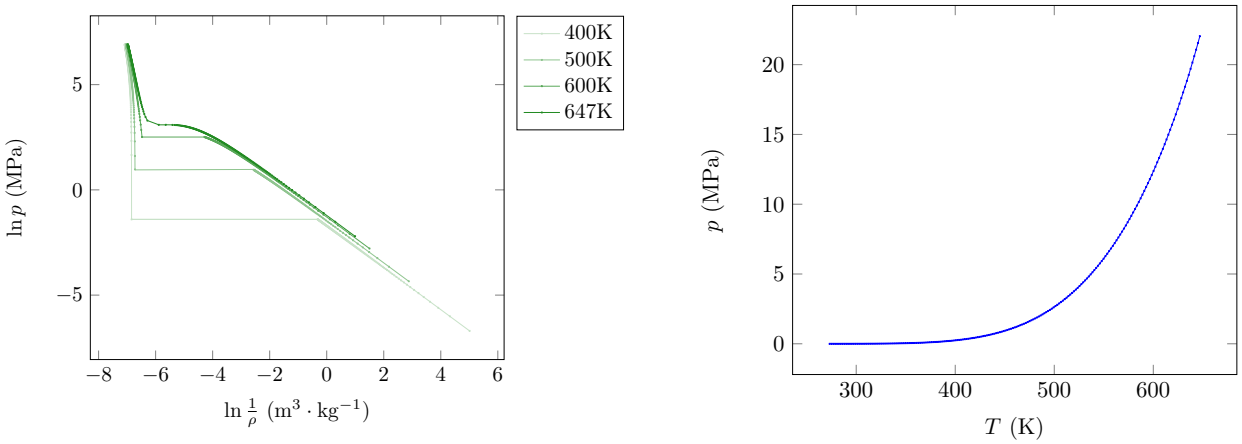

(a) Isotherms in the $(1/\varrho, p)$ plane

(b) Coexistence curve in the (T, p) plane

Figure 4: Saturation and coexistence curves using experimental data from [39]

κ	$\widehat{h}_\kappa$ [kJ · kg^{-1}]	$\widehat{\varrho}_\kappa$ [kg · m^{-3}]	$\widehat{T}_\kappa$ [K]	$\widehat{c}^*_\kappa$ [m · s^{-1}]	$\widehat{c}_{p_\kappa}$ [J · kg^{-1} · K^{-1}]	$\widehat{c}_{v\kappa}$ [J · kg^{-1} · K^{-1}]	$\widehat{\lambda}_\kappa$ [W · m^{-1} · K^{-1}]	$\widehat{\mu}_\kappa$ [Pa · s]
ℓ	978.702	842.783	500.000	1293.67	4561.5	3218.0	0.657	1.209×10^{-4}
ℓ	980.223	842.359	500.336	1292.50	4563.5	3217.0	0.657	1.207×10^{-4}
⋮	⋮	⋮	⋮	⋮	⋮	⋮	⋮	⋮
ℓ	1627.450	595.733	617.667	624.66	8871.0	3098.1	0.459	6.850×10^{-5}
ℓ	$\widehat{h}^s_\ell$	$\widehat{\varrho}^s_\ell$	$\widehat{T}^s$	621.43	8950.0	3101.0	0.458	6.833×10^{-5}
g	$\widehat{h}^s_g$	$\widehat{\varrho}^s_g$	$\widehat{T}^s$	433.40	14 000.6	3633.1	0.121	2.311×10^{-5}
g	2596.965	101.816	618.00	433.69	13 931.7	3627.6	0.121	2.310×10^{-5}
⋮	⋮	⋮	⋮	⋮	⋮	⋮	⋮	⋮
g	3066.962	60.540	699.667	573.70	3670.7	2173.2	0.0803	2.615×10^{-5}
g	3068.184	60.473	700.000	574.02	3664.7	2171.5	0.0803	2.616×10^{-5}

Table 1: Sample of water values [39] at $p_* = 15.5\,\mathrm{MPa}$ with data at saturation $\widehat{h}^s_\ell = 1629.880\,\mathrm{kJ\cdot kg^{-1}}$; $\widehat{h}^s_g = 2596.119\,\mathrm{kJ\cdot kg^{-1}}$; $\widehat{\varrho}^s_\ell = 594.379\,\mathrm{kg\cdot m^{-3}}$; $\widehat{\varrho}^s_g = 101.930\,\mathrm{kg\cdot m^{-3}}$; $\widehat{T}^s = 617.939\,\mathrm{K}$

where six constant parameters have to be tuned: $\overline{c}_v$, $\overline{Q}$, $\overline{\pi}$, $\overline{\gamma}$, $\overline{\mathcal{S}}_0$ and $\overline{b}$ ($\overline{b} = 0$ for the SG law). The tuning depends on the range of enthalpy values and on the phase under consideration. More details on these complete EOS are given in Appendix A. In particular, examples of values for all parameters are given in Table 8. Temperature at saturation T^s is deduced from the equality of Gibbs potentials associated to (6) in the liquid and in the vapour. Enthalpies at saturation are given by $h^s_\kappa = \overline{q}_\kappa + \overline{\gamma}_\kappa \overline{c}_{v\kappa} T^s$. All saturation values are given in Table 4.

SG and NASG laws lead to the same expression for the density

$$\frac{1}{\widetilde{\varrho}(h)} = \frac{\widetilde{\beta}(h)}{p_*}\big(h - \widetilde{q}(h)\big). \tag{7a}$$

The phasewise constant compressibility coefficient is defined by

$$\widetilde{\beta}(h) = \begin{cases} \overline{\beta}_\ell, & \text{if } h \le h^s_\ell, \\ \overline{\beta}_{\text{m}}, & \text{if } h^s_\ell < h < h^s_g, \\ \overline{\beta}_g, & \text{if } h \ge h^s_g, \end{cases} \tag{7b}$$

where $\overline{\beta}_{\text{m}}$ is given by (5a) and

$$\widetilde{q}(h) = \begin{cases} \overline{q}_\ell, & \text{if } h \le h^s_\ell, \\ \overline{q}_{\text{m}}, & \text{if } h^s_\ell < h < h^s_g, \\ \overline{q}_g, & \text{if } h \ge h^s_g, \end{cases} \tag{7c}$$

with $\overline{q}_m$ defined in (5c). For our study, SG [37] and NASG [38] EOS only differ from the values of constant parameters $\overline{\beta}_\kappa$ and $\overline{q}_\kappa$ which are given in Table 5. Let us mention that Hypothesis 3.1-2 reduces in that case to $h_{min} > \overline{q}_\ell$. Hence those analytical EOS are defined over $(0, +\infty)$ since $\overline{q}_\ell < 0$.

❸ **NIST-p**: A sample of tabulated values is given in Table 1 over the range (h_{min}, h_{max}) with

$$h_{min} = 978.702\,\mathrm{kJ\cdot kg^{-1}} \quad \text{and} \quad h_{max} = 3068.184\,\mathrm{kJ\cdot kg^{-1}}.$$

We remark that β does not belong to the set of variables referenced in NIST tables. Consequently, we have to find out a strategy to express the compressibility coefficient. One could have used Formula (2) to define β from the fitting function $h \mapsto \widetilde{\rho}(h)$. Deriving the fitting function would raise some stability issues as well as positivity problems. One may also think of a finite-difference approximation of (2) but that would violate the consistency of thermodynamics (see [43] for more details). This is why we propose here an innovative idea which consists in deriving another expression for β involving tabulated variables but no derivative. From such an expression of β, we shall then deduce a consistent expression for ϱ. We shall see how this idea solves all the aforementioned issues.

Proposition 3.1. *In a pure phase, the compressibility coefficient β satisfies the relation*

$$\beta = \frac{p}{\varrho c^* \sqrt{T}} \sqrt{\frac{1}{c_v} - \frac{1}{c_p}} > 0, \tag{8}$$

where p is the pressure, ϱ the density, T the temperature, c^* the speed of sound, c_v the isochoric heat capacity and c_p the isobaric heat capacity.

Let us observe that, by construction, β is positive. Moreover, this relation is satisfied by the *Stiffened Gas*/*Noble-Abel – Stiffened Gas* laws.

Remark 3.1. *Let us introduce the Joule-Thomson coefficient $\left.\frac{\partial T}{\partial p}\right|_h$ which is also provided in the NIST tables. Then we have the following additional relation, that also enables to compute β from tabulated data:*

$$\beta = \frac{p}{T}\left(\left.\frac{\partial T}{\partial p}\right|_h + \frac{\tau}{c_p}\right). \tag{9}$$

Computations show that similar numerical results are obtained when using (9) or (8).

The proof of Proposition 3.1 and of expression (9) can be found in Appendix B.

Proposition 3.1 is crucial insofar as it enables to provide tabulated values $(\widehat{\beta}_\kappa)_i$ given pointwise values $(\widehat{\varrho}_\kappa)_i$, $(\widehat{T}_\kappa)_i$, $(\widehat{c}^*_\kappa)_i$, $(\widehat{c}_{v_\kappa})_i$ and $(\widehat{c}_{p_\kappa})_i$ for each phase $\kappa \in \{\ell, g\}$. Consequently, we can determine the functions

$$h \mapsto \widetilde{\beta}_\kappa(h) = \sum_{j=0}^{d_{\beta,\kappa}} b_{\kappa,j} \left(\frac{h}{10^6}\right)^j \quad \kappa \in \{\ell, g\}, \tag{10}$$

as adequate fitting polynomials over the intervals $\mathcal{H}_\ell \overset{\text{def}}{=} (h_{min}, \widehat{h}^s_\ell)$ and $\mathcal{H}_g \overset{\text{def}}{=} (\widehat{h}^s_g, h_{max})$ matching the resulting values $(\widehat{\beta}_\kappa)_i$ in each phase.

Any numerical method can be used to determine the fitting polynomials (degrees $d_{\beta,\kappa}$ and coefficients $b_{\kappa,j}$) **providing that it ensures the positivity of both functions** $\widetilde{\beta}_\ell$ and $\widetilde{\beta}_g$, since the values $(\widehat{\beta}_\kappa)_i$ are positive according to (8). In the present work, we apply a least-square regression technique. Degrees of the polynomial were increased until an expected accuracy was reached, *i.e.* when the relative errors defined by

$$\frac{\max_i \left|\widetilde{\beta}_\kappa(h_i) - (\widehat{\beta}_\kappa)_i\right|}{\max_i (\widehat{\beta}_\kappa)_i}$$

are smaller than a chosen threshold. For example, coefficients obtained for a threshold of 10^{-2} at $p_* = 15.5\,\text{MPa}$, as well as the values of the corresponding relative errors, are given in Table 2(a). The resulting function (10) is plotted on Figure 5(a). It can be noticed on Figure 5(a) that for the least-square method we used here, $\widetilde{\beta}_\ell$ and $\widetilde{\beta}_g$ are positive over $\mathcal{H}_\ell$ and $\mathcal{H}_g$. There is a large variety of fitting procedures in the literature which are a lot more accurate than the least-square method. However, we do not need here this level of accuracy, since the relative errors we obtain are satisfactory for our applications. Notice that interpolation methods where the fitting function must match the sampled values are not mandatory here, since β is globally discontinuous.

Hence the global expression of $\widetilde{\beta}$ is given by

$$\widetilde{\beta}(h) = \begin{cases} \widetilde{\beta}_\ell(h), & \text{if } h \leq \widehat{h}^s_\ell, \\ \widetilde{\beta}_m(h) \overset{\text{def}}{=} \overline{\beta}_m, & \text{if } \widehat{h}^s_\ell < h < \widehat{h}^s_g, \\ \widetilde{\beta}_g(h), & \text{if } h \geq \widehat{h}^s_g, \end{cases} \tag{11}$$

where $\overline{\beta}_m$ is given by (5a) with $(h^s_\kappa, \varrho^s_\kappa)$ replaced by $(\widehat{h}^s_\kappa, \widehat{\varrho}^s_\kappa)$ (see corresponding data in Table 4). Orders of magnitude of $\widetilde{\beta}_\kappa$ are given in the third column of Table 5.

Observe that the second item in Hypothesis 3.1 is satisfied by the chosen range of enthalpies, since

$$h_{min} = 9.787 \times 10^5\,\text{J}\cdot\text{kg}^{-1} > \widehat{h}^s_\ell - \frac{p_*}{\widehat{\varrho}^s_\ell \widetilde{\beta}(\widehat{h}^s_\ell)} = 5.646 \times 10^5\,\text{J}\cdot\text{kg}^{-1}.$$

	$\kappa=\ell$	$\kappa=g$
$d_{\beta,\kappa}$	6	3
$b_{\kappa,0}$	$6.129\,697\,412\times10^{-2}$	$-5.395\,575\,381\times10^{-1}$
$b_{\kappa,1}$	$-1.378\,946\,053\times10^{-1}$	$3.591\,468\,350\times10^{-1}$
$b_{\kappa,2}$	$8.329\,391\,618\times10^{-2}$	$9.759\,257\,397\times10^{-3}$
$b_{\kappa,3}$	$6.045\,509\,171\times10^{-3}$	$-1.465\,520\,061\times10^{-2}$
$b_{\kappa,4}$	$2.341\,456\,057\times10^{-2}$	
$b_{\kappa,5}$	$-4.623\,916\,770\times10^{-2}$	
$b_{\kappa,6}$	$1.637\,507\,485\times10^{-2}$	
Error	$6.718\,624\,276\times10^{-3}$	$3.328\,803\,232\times10^{-3}$

(a) Coefficients for $\widetilde{\beta}_\kappa$.

	$\kappa=\ell$	$\kappa=g$
$d_{\varrho,\kappa}$	7	4
$r_{\kappa,0}$	$-0.155\,983\,180\times10^{-3}$	$2.916\,351\,682\times10^{-2}$
$r_{\kappa,1}$	$3.954\,643\,492\times10^{-3}$	$-3.481\,016\,375\times10^{-2}$
$r_{\kappa,2}$	$-4.448\,213\,074\times10^{-3}$	$1.158\,538\,178\times10^{-2}$
$r_{\kappa,3}$	$1.791\,267\,015\times10^{-3}$	$2.098\,765\,032\times10^{-4}$
$r_{\kappa,4}$	$9.750\,821\,242\times10^{-5}$	$-2.363\,742\,034\times10^{-4}$
$r_{\kappa,5}$	$3.021\,233\,622\times10^{-4}$	
$r_{\kappa,6}$	$-4.971\,953\,517\times10^{-4}$	
$r_{\kappa,7}$	$1.509\,223\,489\times10^{-4}$	
Error	$8.627\,504\,234\times10^{-5}$	$9.467\,155\,751\times10^{-5}$

(b) Coefficients for $1/\widetilde{\varrho}_\kappa$.

Table 2: Coefficients of fitting polynomials in the NIST-p strategy at $p_*=15.5\,\mathrm{MPa}$.

Let us now focus on a consistent construction of the density variable by integrating $\widetilde{\beta}_\kappa$ using (2), which also reads $\frac{\partial}{\partial h}\left(\frac{1}{\widetilde{\varrho}}\right)=\frac{\widetilde{\beta}(h)}{p_*}$:

$$\frac{1}{\widetilde{\varrho}(h)}=\begin{cases}\dfrac{1}{\widetilde{\varrho}_\ell(h)}\overset{\text{def}}{=}\dfrac{1}{\widehat{\varrho}^s_\ell}+\displaystyle\int_{\widehat{h}^s_\ell}^{h}\frac{\widetilde{\beta}_\ell(\mathfrak{h})}{p_*}\mathrm{d}\mathfrak{h}, & \text{if } h\le\widehat{h}^s_\ell,\\ \dfrac{1}{\varrho_{\mathrm{m}}(h)}, & \text{if } \widehat{h}^s_\ell<h<\widehat{h}^s_g,\\ \dfrac{1}{\widetilde{\varrho}_g(h)}\overset{\text{def}}{=}\dfrac{1}{\widehat{\varrho}^s_g}+\displaystyle\int_{\widehat{h}^s_g}^{h}\frac{\widetilde{\beta}_g(\mathfrak{h})}{p_*}\mathrm{d}\mathfrak{h}, & \text{if } h\ge\widehat{h}^s_g,\end{cases}\tag{12}$$

where ϱ_{m} is defined by (5b).[8] We write in a global way

$$\frac{1}{\widetilde{\varrho}_\kappa(h)}=\sum_{j=0}^{d_{\varrho,\kappa}}r_{\kappa,j}\left(\frac{h}{10^6}\right)^j,\tag{13}$$

where the coefficients are stored in Table 2(b) and the curves are plotted on Figure 5(b). The values of the relative errors are also given in Table 2(b). Obviously $d_{\varrho,\kappa}=d_{\beta,\kappa}+1$.

By construction, the following properties are satisfied:

Proposition 3.2. *Provided that $\widetilde{\beta}_\ell$ and $\widetilde{\beta}_g$ are positive, the density $\widetilde{\varrho}$ defined by (12) is such that*

(a) Under Hypothesis 3.1-2., $h\mapsto\widetilde{\varrho}(h)$ is positive over (h_{min},h_{max});

(b) $h\mapsto\widetilde{\varrho}(h)$ is continuous over (h_{min},h_{max}) and satisfies exactly the tabulated values at saturation; in particular, $\widetilde{\varrho}_\kappa(\widehat{h}^s_\kappa)=\varrho_{\mathrm{m}}(\widehat{h}^s_\kappa)=\widehat{\varrho}^s_\kappa$, $\kappa\in\{\ell,g\}$;

(c) $h\mapsto\widetilde{\varrho}(h)$ is decreasing over (h_{min},h_{max});

(d) Relation (2) exactly holds.

These properties are of great importance in thermodynamics and they would not have been fulfilled necessarily by a fitting of the density using only the values $(\widehat{\varrho}_\kappa)_i$.

A straightforward consequence of this proposition is that $h\mapsto\widetilde{\varrho}(h)$ is invertible, which in particular enables to determine a unique h_e such that $\widetilde{\varrho}(h_e)=\varrho_e$ (cf. Hypothesis 3.1-1.).

❹ **NIST-0**: In the previous strategy, degrees $d_{\beta,\kappa}$ of the fitting polynomials were chosen large enough to make the approximation error as small as expected. However it is also possible to choose $d_{\beta,\kappa}=0$ to construct a phasewise approximation like (11) but with constant phase functions $\widetilde{\beta}_\kappa(h)\equiv\overline{\beta}_\kappa$. We choose here the average between the minimal and the maximal value in each phase

$$\overline{\beta}_\kappa\overset{\text{def}}{=}\frac{\min_i\left(\widehat{\beta}_\kappa\right)_i+\max_i\left(\widehat{\beta}_\kappa\right)_i}{2}>0,\quad\kappa\in\{\ell,g\},\tag{14a}$$

[8] In particular, the definition of ϱ_{m} ensures that $\dfrac{1}{\varrho_{\mathrm{m}}(h)}=\dfrac{1}{\widehat{\varrho}^s_\ell}+\displaystyle\int_{\widehat{h}^s_\ell}^{h}\frac{\overline{\beta}_{\mathrm{m}}}{p_*}\mathrm{d}\mathfrak{h}=\frac{1}{\widehat{\varrho}^s_g}+\int_{\widehat{h}^s_g}^{h}\frac{\overline{\beta}_{\mathrm{m}}}{p_*}\mathrm{d}\mathfrak{h}$.

	$\kappa = \ell$	$\kappa = g$
$d_{\varrho,\kappa}$	1	1
$r_{\kappa,0}$	7.416×10^{-5}	-2.643×10^{-2}
$r_{\kappa,1}$	9.867×10^{-10}	1.396×10^{-8}

Table 3: Coefficients for $1/\widetilde{\varrho}_\kappa$ in the NIST-0 strategy

	❶ SG	❷ NASG	❸-❹ NIST [39]
h_ℓ^s	$1.627 \times 10^6\,\mathrm{J \cdot kg^{-1}}$	$1.596 \times 10^6\,\mathrm{J \cdot kg^{-1}}$	$\widehat{h}_\ell^s$
h_g^s	$3.004 \times 10^6\,\mathrm{J \cdot kg^{-1}}$	$2.861 \times 10^6\,\mathrm{J \cdot kg^{-1}}$	$\widehat{h}_g^s$
ϱ_ℓ^s	$632.663\,\mathrm{kg \cdot m^{-3}}$	$737.539\,\mathrm{kg \cdot m^{-3}}$	$\widehat{\varrho}_\ell^s$
ϱ_g^s	$52.937\,\mathrm{kg \cdot m^{-3}}$	$55.486\,\mathrm{kg \cdot m^{-3}}$	$\widehat{\varrho}_g^s$
T^s	654.65 K	636.47 K	$\widehat{T}^s$

Table 4: Values at saturation for $p_* = 15.5\,\mathrm{MPa}$ found in the NIST tables [39], or deduced from the parameters of [37] for SG and of [38] for NASG.

and $\overline{\beta}_{\mathrm{m}}$ as in (5a) with $(h_\kappa^s, \varrho_\kappa^s)$ replaced by $(\widehat{h}_\kappa^s, \widehat{\varrho}_\kappa^s)$. Resulting values are given in the fourth column of Table 5. We then apply the same construction (12) for the density as in the NIST-p strategy. In this phasewise constant case, we notice that this construction procedure leads to an expression of the density which is similar to the (NA)SG law (7), namely

$$\frac{1}{\widetilde{\varrho}(h)} = \frac{\widetilde{\beta}(h)}{p_*}\big(h - \widetilde{q}(h)\big), \tag{14b}$$

where

$$\widetilde{q}(h) = \begin{cases} \overline{q}_\ell \overset{\text{def}}{=} \widehat{h}_\ell^s - \dfrac{1}{\widehat{\varrho}_\ell^s}\dfrac{p_*}{\overline{\beta}_\ell}, & \text{if } h \le \widehat{h}_\ell^s, \\ \overline{q}_{\mathrm{m}}, & \text{if } \widehat{h}_\ell^s < h < \widehat{h}_g^s, \\ \overline{q}_g \overset{\text{def}}{=} \widehat{h}_g^s - \dfrac{1}{\widehat{\varrho}_g^s}\dfrac{p_*}{\overline{\beta}_g}, & \text{if } h \ge \widehat{h}_g^s, \end{cases} \tag{14c}$$

with $\overline{q}_{\mathrm{m}}$ defined by (5c). The values of $\overline{q}_\kappa$ are stored in Table 5, those of $\widehat{\varrho}_\kappa^s$ and $\widehat{h}_\kappa^s$ are given in the caption of Table 1 and coefficients of the polynomials $1/\widetilde{\varrho}_\kappa$ in Table 3. It is straightforward that Proposition 3.2 still holds for the NIST-0 strategy.

With our construction, the saturation is exactly satisfied, unlike EOS obtained with parameters of [37] for SG or with parameters of [38] for NASG. Nevertheless, observe that the NIST-p/NIST-0 EOS are not complete equations of state, so that we cannot use these laws in a compressible model, However, it is the simplest and most accurate analytical law to obtain an exact analytical solution not only for the steady 1D Lmnc model but also for transient versions. The four strategies will be compared below (see § 4.3). The comparison shows that assuming β to be constant is not a restriction, but that the most crucial point is to satisfy accurately the saturation.

In conclusion, the definitions $\widetilde{\beta}$ and $\widetilde{\varrho}$ depending on the EOS are summarised in Table 6.

3.2 Viscosity coefficients

We also have to specify how to compute the viscosity coefficients in the stress tensor involved in (1c). Let μ and η be respectively the dynamic and bulk viscosities. As previously, we split the modelling into three parts corresponding to each phase. More precisely, we set:

$$\widetilde{\mu}(h) = \begin{cases} \widetilde{\mu}_\ell(h), & \text{if } h \le h_\ell^s, \\ \widetilde{\mu}_{\mathrm{m}}(h) \overset{\text{def}}{=} \widetilde{\alpha}(h)\widetilde{\mu}_g\big(h_g^s\big) + \big(1 - \widetilde{\alpha}(h)\big)\widetilde{\mu}_\ell\big(h_\ell^s\big), & \text{if } h_\ell^s < h < h_g^s, \\ \widetilde{\mu}_g(h), & \text{if } h \ge h_g^s. \end{cases}$$

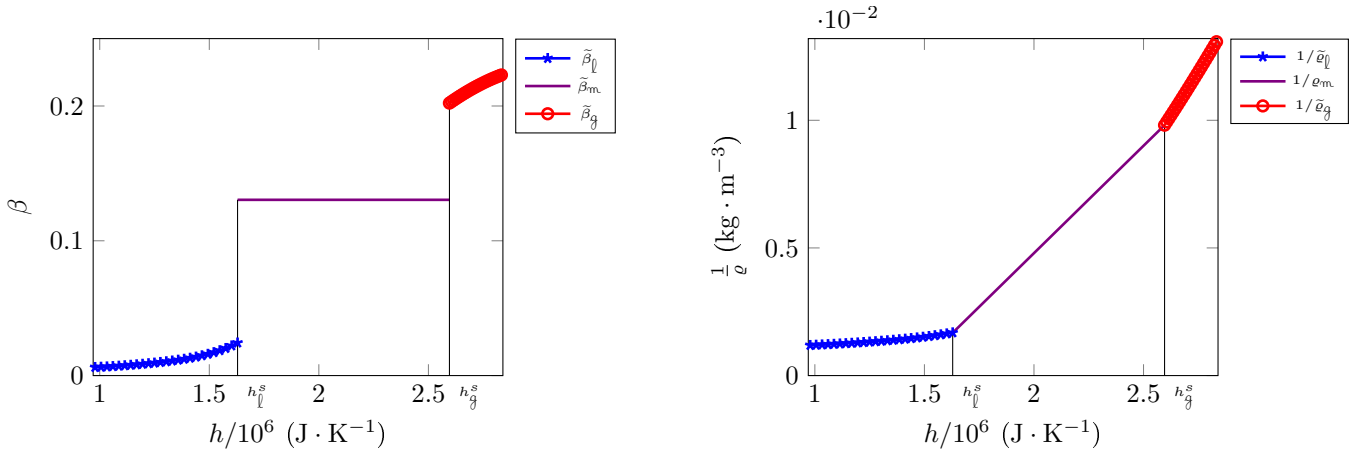

(a) Compressibility coefficient.

(b) Specific volume.

Figure 5: Fitting polynomials for compressibility coefficient (Tab. 2a) and specific volume (Tab. 2b).

	❶ SG	❷ NASG	❸ NIST-p	❹ NIST-0
$\widetilde{\beta}_\ell$	8.769×10^{-3}	4.803×10^{-3}	6.143×10^{-3} to 2.437×10^{-2}	1.529×10^{-2}
$\overline{\beta}_m$	1.949×10^{-1}	2.042×10^{-1}	1.303×10^{-1}	1.303×10^{-1}
$\widetilde{\beta}_\vartheta$	3.007×10^{-1}	4.872×10^{-1}	2.022×10^{-1} to 2.310×10^{-1}	2.163×10^{-1}
$\overline{q}_\ell$	-1.167×10^6 J · kg^{-1}	-2.779×10^6 J · kg^{-1}	N/A	-7.654×10^4 J · kg^{-1}
$\overline{q}_m$	1.501×10^6 J · kg^{-1}	1.493×10^6 J · kg^{-1}	1.429×10^6 J · kg^{-1}	1.429×10^6 J · kg^{-1}
$\overline{q}_\vartheta$	2.030×10^6 J · kg^{-1}	2.287×10^6 J · kg^{-1}	N/A	1.893×10^6 J · kg^{-1}

Table 5: Orders of magnitude of the compressibility coefficient β and the equivalent binding energy q at $p_* = 15.5$ MPa. For pure phases: values obtained thanks to (8) using NIST tables [39], or using formulae introduced in [2] for SG and NASG. For values in the mixture: values given by (5a) and (5c).

Law	❶ SG and ❷ NASG	❸ NIST-p	❹ NIST-0
$\widetilde{\beta}$	(7b)-(5a)	(11)-(10)-(5a)	(11)-(14a)-(5a)
$\widetilde{\rho}$	(7)-(5)	(12)-(13)-(5)	(14)-(5)

Table 6: Definitions $\widetilde{\beta}$ and $\widetilde{\varrho}$ depending on the EOS

As for the bulk viscosity, we take $\widetilde{\eta}(h) = -\frac{2}{3}\widetilde{\mu}(h)$ under the Stokes hypothesis. The expression in the mixture is defined by means of a linear approximation involving the volume fraction α, given by

$$\widetilde{\alpha}(h) = \begin{cases} 0, & \text{if } h \leq h_{\ell}^{s}, \\ \dfrac{\left(h - h_{\ell}^{s}\right)\varrho_{\ell}^{s}}{\varrho_{g}^{s}h_{g}^{s} - \varrho_{\ell}^{s}h_{\ell}^{s} - (\varrho_{g}^{s} - \varrho_{\ell}^{s})h}, & \text{if } h_{\ell}^{s} < h < h_{g}^{s}, \\ 1, & \text{if } h \geq h_{g}^{s}. \end{cases}$$

As for other NIST data, the viscosity could be approximated by a polynomial expression $\widetilde{\mu}_{\kappa}(h)$ fitting tabulated values, for example by means of a least-square regression technique. However, due to the weak variability of the viscosity, we approximate μ by a phasewise constant function, also computed from the NIST data, as the average between the minimal and the maximal value in each phase

$$\widetilde{\mu}_{\ell}(h) \equiv \overline{\mu}_{\ell} = 9.462 \times 10^{-5}\,\mathrm{Pa}\cdot\mathrm{s}, \qquad \widetilde{\mu}_{g}(h) \equiv \overline{\mu}_{g} = 2.464 \times 10^{-5}\,\mathrm{Pa}\cdot\mathrm{s}.$$

3.3 Thermal effects

Low Mach number models allow to deal with large heat transfers unlike incompressible models. It is thus interesting to investigate the influence of the thermal conductivity.

Since the temperature is constant within the mixture phase, T is not an appropriate unknown for the modelling of phase transition at this scale. This is why we rather expressed the model in terms of enthalpy, which is not constant in the mixture phase. Let us denote by λ the thermal conductivity of water. We mention that this physical variable is referenced in the NIST tables (see Table 1). Then the classic term $\nabla\cdot(\lambda\nabla T)$ which models heat conduction (Fourier's law) becomes in a pure phase $\nabla\cdot(\Lambda\nabla h)$, where Λ is defined by

$$\Lambda \overset{\text{def}}{\equiv} \frac{\lambda}{c_p}.$$

As previously, c_p is the isochoric heat capacity (defined by (23) or (26)), which is involved in the classic thermodynamic equality $\mathrm{d}h = c_p\mathrm{d}T$. We the, define Λ over the whole range of enthalpy values by

$$\widetilde{\Lambda}(h) = \begin{cases} \widetilde{\lambda}_{\ell}(h) \times \left(\widetilde{\frac{1}{c_p}}\right)_{\ell}(h), & \text{if } h \leq \widehat{h}_{\ell}^{s}, \\ 0, & \text{if } \widehat{h}_{\ell}^{s} < h < \widehat{h}_{g}^{s}, \\ \widetilde{\lambda}_{g}(h) \times \left(\widetilde{\frac{1}{c_p}}\right)_{g}(h), & \text{if } h \geq \widehat{h}_{g}^{s}. \end{cases} \tag{15}$$

The coefficient is set to 0 for $h \in (h_{\ell}^{s}, h_{g}^{s})$ because the temperature is constant within the mixture phase, and there is no thermal conduction therein.

Isobaric heat coefficient To construct functions $\left(\widetilde{1/c_p}\right)_{\kappa}$ ($\kappa \in \{\ell, g\}$), we may use the same strategies as in § 3.1.2 for the computation of β, namely ❶-❷ for the SG/NASG EOS, ❸ for high-order polynomial-fitting and ❹ for constant approximations. In the cases ❶-❷, the heat coefficients are constant and given by

$$\overline{c_p}_{\kappa} = \overline{\gamma}_{\kappa}\overline{c_v}_{\kappa}, \tag{16}$$

$\kappa \in \{\ell, g\}$, with values of parameters $\overline{\gamma}_{\kappa}$ and $\overline{c_v}_{\kappa}$ recalled in Table 8.

For strategies ❸-❹, a least-square regression technique is used to fit values from the NIST tables [39]:

$$h \mapsto \left(\widetilde{\frac{1}{c_p}}\right)_{\kappa}(h) = \sum_{j=0}^{d_{c_p,\kappa}} c_{\kappa,j}\left(\frac{h}{10^6}\right)^{j}. \tag{17}$$

Note that we decided to fit $1/c_p$ instead of c_p since it appears as such in the definitions of Λ and of T (see below).

Let us notice that strategies for the computation of β and c_p are decoupled, since we are considering incomplete equations of state. It corresponds to numerical techniques to approximate thermodynamic variables using the most suitable way. In particular, a NIST-0 (for β) – NIST-0 (for $1/c_p$) strategy would mimic the SG-NASG EOS in terms of algebraic formulation (constant) except that constant values are not related to each other. No matter which numerical method one applies in order to fit the NIST values of $1/c_p$, it must be ensured that the resulting function is positive over (h_{min}, h_{max}). In the present case, we decided to apply a NIST-p strategy, whose coefficients are given in Table 7(a), and the curves can be seen on Figure 6(a).

	$\kappa = \ell$	$\kappa = g$
$d_{c_p,\kappa}$	7	6
$c_{\kappa,0}$	$1.689\,602\,951 \times 10^{-4}$	$5.382\,374\,281 \times 10^{-4}$
$c_{\kappa,1}$	$1.232\,572\,675 \times 10^{-4}$	$-2.539\,666\,705 \times 10^{-4}$
$c_{\kappa,2}$	$2.380\,465\,421 \times 10^{-5}$	$-2.690\,479\,385 \times 10^{-4}$
$c_{\kappa,3}$	$-1.311\,465\,424 \times 10^{-4}$	$1.079\,811\,811 \times 10^{-4}$
$c_{\kappa,4}$	$-1.531\,310\,649 \times 10^{-5}$	$1.163\,418\,815 \times 10^{-5}$
$c_{\kappa,5}$	$6.360\,562\,483 \times 10^{-5}$	$-3.873\,402\,400 \times 10^{-7}$
$c_{\kappa,6}$	$-7.958\,443\,754 \times 10^{-6}$	$-1.196\,179\,285 \times 10^{-6}$
$c_{\kappa,7}$	$-7.446\,866\,275 \times 10^{-6}$	
Error	$2.840\,610\,126 \times 10^{-3}$	$1.731\,914\,106 \times 10^{-3}$

(a) Coefficients for $\left(\widetilde{\frac{1}{c_p}}\right)_\kappa$.

	$\kappa = \ell$	$\kappa = g$
$d_{T,\kappa}$	8	7
$t_{\kappa,0}$	293.445 144 7	300.584 284 2
$t_{\kappa,1}$	168.960 295 1	538.237 428 1
$t_{\kappa,2}$	61.628 633 75	$-126.983\,335\,2$
$t_{\kappa,3}$	7.934 884 737	$-89.682\,646\,17$
$t_{\kappa,4}$	$-32.786\,635\,60$	26.995 295 28
$t_{\kappa,5}$	$-3.062\,621\,298$	2.326 837 630
$t_{\kappa,6}$	10.600 937 47	$-6.455\,670\,667 \times 10^{-2}$
$t_{\kappa,7}$	$-1.136\,920\,536$	$-1.708\,827\,550 \times 10^{-1}$
$t_{\kappa,8}$	$-0.930\,858\,284\,4$	
Error	$7.340\,188\,470 \times 10^{-6}$	$4.820\,515\,518 \times 10^{-6}$

(b) Coefficients for $\widetilde{T}_\kappa$.

Table 7: Coefficients of fitting polynomials in the NIST-p strategy at $p_* = 15.5\,\mathrm{MPa}$.

Temperature Although the temperature is not involved in the LMNC system (1), it is useful to compute it, in the purpose of analysing numerical results and for safety evaluations. For strategies ❶-❷, the temperature reads

$$\widetilde{T}(h) = \begin{cases} \dfrac{h - \overline{q}_\ell}{\overline{c_p}_\ell}, & \text{if } h \le h^s_\ell, \\ T^s, & \text{if } h^s_\ell < h < h^s_g, \\ \dfrac{h - \overline{q}_g}{\overline{c_p}_g}, & \text{if } h \ge h^s_g, \end{cases}$$

where $\overline{c_p}_\kappa$ was introduced in (16) and $\overline{q}_\kappa$ is stored in Table 5. Values at saturation T^s and h^s_κ are recalled in Table 4. For strategies ❸-❹, similarly to the way we defined the density ρ from the compressibility coefficient β, we deduce the expression of the temperature T by integrating $1/c_p$ from (17) according to (26). Hence

$$\widetilde{T}(h) = \begin{cases} \widetilde{T}_\ell(h) \overset{\text{def}}{=} \widehat{T}^s + \displaystyle\int_{\widehat{h}^s_\ell}^{h} \left(\widetilde{\frac{1}{c_p}}\right)_\ell (\mathfrak{h})\mathrm{d}\mathfrak{h}, & \text{if } h \le \widehat{h}^s_\ell, \\ \widetilde{T}_m(h) \overset{\text{def}}{=} \widehat{T}^s, & \text{if } \widehat{h}^s_\ell < h < \widehat{h}^s_g, \\ \widetilde{T}_g(h) \overset{\text{def}}{=} \widehat{T}^s + \displaystyle\int_{\widehat{h}^s_g}^{h} \left(\widetilde{\frac{1}{c_p}}\right)_g (\mathfrak{h})\mathrm{d}\mathfrak{h}, & \text{if } h \ge \widehat{h}^s_g. \end{cases} \tag{18}$$

We write in a global way

$$\widetilde{T}_\kappa(h) = \sum_{j=0}^{d_{T,\kappa}} t_{\kappa,j} \left(\frac{h}{10^6}\right)^j, \tag{19}$$

where the coefficients are stored in Table 7(b) and the curves are plotted on Figure 6(b). The values of the relative errors are also given in Table 7(b). Obviously $d_{T,\kappa} = d_{c_p,\kappa} + 1$.

This construction automatically ensures the following properties (see Figure 6(b)):

Proposition 3.3. *Provided that* $(\widetilde{1/c_p})_\ell$ *and* $(\widetilde{1/c_p})_g$ *are positive, the temperature* $\widetilde{T}$ *defined by* (18) *satisfies:*

- *Under Hypothesis 3.1.2,* $h \mapsto \widetilde{T}(h)$ *is continuous and positive over* (h_{min}, h_{max})*;*
- $h \mapsto \widetilde{T}(h)$ *is increasing over* (h_{min}, h_{max})*;*[9]
- *The differential relation* (26) *exactly holds.*

[9] $h \mapsto \widetilde{T}(h)$ is constant over $(\widehat{h}^s_\ell, \widehat{h}^s_g)$.

Thermal conductivity Similarly to other NIST data, the thermal conductivity could have been approximated by a polynomial expression $\widetilde{\lambda}_\kappa(h)$ by means of a least-square regression technique. However, due to the weak variability of the thermal conductivity, we approximate λ by a phasewise constant function, also computed from the NIST data as the average between the minimal and the maximal value in each phase:

$$\widetilde{\lambda}_\ell(h) \equiv \overline{\lambda}_\ell = 5.578 \times 10^{-1}\,\mathrm{W}\cdot\mathrm{m}^{-1}\cdot\mathrm{K}^{-1}, \qquad \widetilde{\lambda}_g(h) \equiv \overline{\lambda}_g = 1.008 \times 10^{-1}\,\mathrm{W}\cdot\mathrm{m}^{-1}\cdot\mathrm{K}^{-1}.$$

4 Analytical results on the model and comparison of the EOS

The model we actually address in this work is thus

$$\begin{cases} \nabla\cdot\boldsymbol{u} = \dfrac{\widetilde{\beta}(h)}{p_*}\left[\nabla\cdot\big(\widetilde{\Lambda}(h)\nabla h\big) + \Phi\right], & \text{(20a)}\\ \widetilde{\varrho}(h)\times\left[\partial_t h + \boldsymbol{u}\cdot\nabla h\right] = \nabla\cdot\big(\widetilde{\Lambda}(h)\nabla h\big) + \Phi, \qquad (t,\boldsymbol{x})\in\mathbb{R}^+\times\Omega^d, & \text{(20b)}\\ \widetilde{\varrho}(h)\times\left[\partial_t\boldsymbol{u} + (\boldsymbol{u}\cdot\nabla)\boldsymbol{u}\right] - \nabla\cdot\left[\widetilde{\mu}(h)\left(\nabla\boldsymbol{u} + (\nabla\boldsymbol{u})^T\right)\right] - \nabla\left[\widetilde{\eta}(h)\nabla\cdot\boldsymbol{u}\right] + \nabla\mathcal{P} = \widetilde{\varrho}(h)\boldsymbol{g}, & \text{(20c)}\end{cases}$$

where the expressions of $\widetilde{\beta}$ and $\widetilde{\varrho}$ are detailed in § 3.1, those of $\widetilde{\mu}$ and $\widetilde{\eta}$ in § 3.2 and the one of $\widetilde{\Lambda}$ in § 3.3.

4.1 Jump conditions

Taking into account thermal diffusion modifies the nature of the differential problem in depth. As detailed in § 3.3, $\widetilde{\Lambda}$ defined by (15) is discontinuous when phase transition occurs. Then Equation (20b) – which governs the evolution of the enthalpy – is a degenerate parabolic equation: it reduces to a nonlinear transport equation in the mixture phase. This requires to increase the regularity of h in the variational approach (see § 5.1).

Moreover, the diffusion coefficient is discontinuous across phase transition curves. Consequently, we have to define rigorously the conservative second-order differential term in (20).

Let us introduce some notations. We set

$$\Omega^d_\ell(t) \overset{\text{def}}{=} \{\boldsymbol{x}\in\Omega^d \,:\, h(t,\boldsymbol{x}) < h^s_\ell\}, \quad \Omega^d_m(t) \overset{\text{def}}{=} \{\boldsymbol{x}\in\Omega^d \,:\, h^s_\ell < h(t,\boldsymbol{x}) < h^s_g\} \quad \text{and} \quad \Omega^d_g(t) \overset{\text{def}}{=} \{\boldsymbol{x}\in\Omega^d \,:\, h(t,\boldsymbol{x}) > h^s_g\}$$

the domains occupied by each phase. Each of them may be an empty set depending on the evolution of h.

Phase domains are separated by level sets of the enthalpy

$$\Gamma_\ell(t) = \{\boldsymbol{x}\in\Omega^d \,:\, h(t,\boldsymbol{x}) = h^s_\ell\} \quad \text{and} \quad \Gamma_g(t) = \{\boldsymbol{x}\in\Omega^d \,:\, h(t,\boldsymbol{x}) = h^s_g\}.$$

From now on, a solution $(h,\boldsymbol{u},\mathcal{P})$ to System (20) must be understood as follows:

- In each phase domain $\Omega^d_\kappa(t)$, $(h,\boldsymbol{u},\mathcal{P})(t,\cdot)$ is a strong solution.
- Where phase transition occurs, we impose the following jump conditions over $\Gamma_\ell(t)$ and $\Gamma_g(t)$

$$\left[\!\left[\widetilde{\Lambda}(h)\nabla h\right]\!\right]\cdot\boldsymbol{n} = 0, \tag{21a}$$

$$\left[\!\left[\widetilde{\mu}(h)\left(\nabla\boldsymbol{u} + (\nabla\boldsymbol{u})^T\right) + \widetilde{\eta}(h)(\nabla\cdot\boldsymbol{u})\mathcal{I}_d - \mathcal{P}\mathcal{I}_d\right]\!\right]\boldsymbol{n} = 0. \tag{21b}$$

- Moreover, h satisfies the continuity condition

$$[\![h]\!] = 0 \tag{21c}$$

only where the flow goes into the mixture phase, *i.e.* over $\bigcup_{\kappa\in\{\ell,g\}}\{\boldsymbol{x}\in\Gamma_\kappa(t) \,:\, \boldsymbol{u}(t,\boldsymbol{x})\cdot\boldsymbol{n}_m(t,\boldsymbol{x}) > 0\}$, where $\boldsymbol{n}_m$ is the normal vector pointing towards the mixture phase.

This problem can be considered a coupling issue between two models: one of hyperbolic nature, one of parabolic nature. Such a coupling has been investigated in the literature (*e.g.* [55, 56]) but in the case of fixed boundaries. An additional obstacle in the present case is that the discontinuity location moves with time (level set of the enthalpy). The theoretical analysis of the model (20-3-21) is left to future works.

4.2 Assumptions

For the problem to be well-posed, we impose some assumptions upon the data. We first suppose that physical data satisfy:

Hypothesis 4.1.

1. *For all* $(t, \boldsymbol{x}) \in \mathbb{R}^+ \times \Omega^d$, $\Phi(t, \boldsymbol{x})$ *is non-negative.*
2. *For all* $(t, x) \in \mathbb{R}^+ \times [0, L_x]$, $D_e(t, x)$ *is non-negative.*
3. p_* *is a positive constant.*

The first assumption characterises the fact that we study a nuclear core where the coolant fluid is heated. In a nuclear power plant of PWR or BWR type, water is injected at the bottom of the core with a positive velocity, which is the meaning of the second assumption. Notice that D_e can be compactly supported in $(x_1, x_2) \subset (0, L_x)$.
We make the following modelling hypothesis which somehow restricts the range of experiments as we cannot predict the orientation of the output velocity field.

Hypothesis 4.2. *The velocity field is outgoing,* i.e. $\boldsymbol{u} \cdot \boldsymbol{n}(t, \boldsymbol{x})|_{y=L_y} > 0$ *for all* $(t, \boldsymbol{x}) \in \mathbb{R}^+ \times \Omega^d$.

This hypothesis is necessary because no Dirichlet boundary conditions is imposed at the exit of the core upon the enthalpy. It induces that no downward flow (recirculation) occurs at the exit. In dimension 1 when $\widetilde{\Lambda} \equiv 0$, Hypothesis 4.2 is a direct consequence of Hypothesis 4.1 and of the positivity of β; in dimensions 2 and 3, Hypothesis 4.2 is needed.

4.3 Influence of the equation of state on 1D steady states

In dimension 1 and without thermal diffusion, we can explicitly compute steady solutions of the Lmnc model, no matter what the equation of state.

Proposition 4.1 (Steady states)**.** *We consider the 1D steady case without thermal diffusion,* i.e. ϱ_e, D_e *and* Φ *do not depend on time and* $\widetilde{\Lambda} \equiv 0$. *Then, System* (20) *admits a unique steady solution, where* h *and* v *are given by*

$$h(y) = \widetilde{\varrho}^{-1}(\varrho_e) + \frac{1}{D_e}\int_0^y \Phi(z)\,\mathrm{d}z, \qquad v(y) = \frac{D_e}{\widetilde{\varrho}(h(y))}.$$

Proof. System (20a)-(20b) reduces to

$$\begin{cases} \partial_y v = -\dfrac{1}{\widetilde{\varrho}(h)^2}\widetilde{\varrho}'(h)\Phi(y), \qquad v(t,0) = D_e/\varrho_e > 0, & \text{(22a)} \\ v\partial_y h = \dfrac{1}{\widetilde{\varrho}(h)}\Phi(y), \qquad h(t,0) = h_e, & \text{(22b)} \end{cases}$$

with h_e such that $\widetilde{\varrho}(h_e) = \varrho_e > 0$. Then

$$\partial_y\big(\widetilde{\varrho}(h)v\big) = \widetilde{\varrho}'(h)v\partial_y h + \widetilde{\varrho}\partial_y v \overset{(22a)}{=} \widetilde{\varrho}'(h)v\partial_y h - \frac{\widetilde{\varrho}'(h)}{\widetilde{\varrho}(h)}\Phi \overset{(22b)}{=} 0.$$

Hence $\widetilde{\varrho}(h(y))v(y) = D_e$ and finally $\partial_y h(y) = \frac{1}{\widetilde{\varrho}(h(y))v(y)}\Phi(y) = \frac{\Phi(y)}{D_e}$. □

Remark 4.1.

1. *A distinctive feature of the* Lmnc *model is that the steady enthalpy does not depend on the equation of state except through the computation of* h_e. *Moreover as* Φ *is non-negative (Hypothesis 4.1), the enthalpy is monotone increasing.*
2. *There is no proof of existence for an asymptotic state of System* (1) *(in the sense* $t \to +\infty$*) in the general case.*[10] *But if such an asymptotic solution exists, it is necessary the one described in Proposition 4.1.*
3. *Given the expression of* h *in Proposition 4.1, it can be stated whether the steady flow involves only (pure) liquid (if* $h(L_y) < h_\ell^s$*) or mixture (*$h_\ell^s \le h(L_y) \le h_g^s$*) or (pure) vapour (*$h(L_y) > h_g^s$*).*

[10] It has been proven for the *Stiffened Gas* law and for simple expressions of Φ in [2].

To compare the influence of the equation of state on the steady solution, we consider values of a pressurised water reactor, with water injected at liquid state:

- thermodynamic pressure: $p_* = 15.5\,\mathrm{MPa}$,
- height of the core: $L = 4.2\,\mathrm{m}$,
- power density: $\Phi_\star = 170 \times 10^6\,\mathrm{W}\cdot\mathrm{m}^{-3}$,
- injection: $v_e = 0.5\,\mathrm{m}\cdot\mathrm{s}^{-1}$[11] and $\varrho_e = 750\,\mathrm{kg}\cdot\mathrm{m}^{-3}$, so that $D_e = 375\,\mathrm{kg}\cdot\mathrm{s}^{-1}\cdot\mathrm{m}^{-2}$.

As mentioned above, the computation of h_e depends on the equation of state. For NIST-0, SG and NASG, the computation is exact: $h_e = \overline{q}_\ell + \frac{p_*}{\overline{\rho}_\ell}\frac{1}{\varrho_e}$. For NIST-p, we have to solve numerically $\varrho(h_e, p_*) = \varrho_e$. We obtain

	❶ SG	❷ NASG	❸ NIST-p	❹ NIST-0
h_e	$1.190 \times 10^6\,\mathrm{J}\cdot\mathrm{kg}^{-1}$	$1.523 \times 10^6\,\mathrm{J}\cdot\mathrm{kg}^{-1}$	$1.274 \times 10^6\,\mathrm{J}\cdot\mathrm{kg}^{-1}$	$1.276 \times 10^6\,\mathrm{J}\cdot\mathrm{kg}^{-1}$

The NIST tables provide an approximate value $h_e = 1.273\,78 \times 10^6\,\mathrm{J}\cdot\mathrm{kg}^{-1}$.

The discrepancy between the four values at $y = 0$ remains the same over the whole domain as the steady solutions $y \mapsto h(y)$ are linear with the same slope (see Figure 7a).

It can also be stated where the fluid is present only as a (pure) liquid phase (if $h(y) < h_\ell^s$) or as a mixture ($h_\ell^s \leq h(y) \leq h_g^s$) or also as a (pure) vapour phase ($h(y) > h_g^s$) by solving level sets $h(y_\kappa^s) = h_\kappa^s$:

	❶ SG	❷ NASG	❸ NIST-p	❹ NIST-0
y_ℓ^s	0.964 m	0.160 m	0.786 m	0.780 m
y_g^s	4.002 m	2.950 m	2.917 m	2.912 m

The errors upon the enthalpies at saturation and at the entrance when the EOS is ill-approximated result in dramatic consequences: the computations with the SG EOS provide a late vaporisation as we can see in the schematic comparison of Figure 7(b), which describes the distribution of pure liquid, steam-water mixture and vapour phases in the reactor core. We therefore highlight the importance of a precise description of the EOS when dealing with safety and design of PWR.

5 Numerical strategy and simulations

5.1 Numerical scheme

Let us first recall what was investigated from the numerical point of view in our previous works with the SG law. In [2], the 1D Lmnc model with phase transition is simulated by means of two distinct numerical schemes based on the method of characteristics. Unconditionally stable, they ensure the positivity of the density. In [4], we derive a 2D weak formulation for the monophasic version of the model in a finite-element framework. It is extended to multiphasic flows in [1] with a weak formulation requiring an interface tracking algorithm.

In this section, we present a new version of the weak formulation which overcomes the previous issues and deals with tabulated values in the context of phase transition. Moreover, thermal conduction is taken into account.

For the transport terms, we use the method of characteristics. This feature is embedded in the Finite-Element software `FreeFem++` [57] through the function `convect`. For reasons described below in Remark 5.1, we do not consider Equation (20a) as such but under the equivalent form

$$\nabla\cdot\boldsymbol{u} = \frac{\widetilde{\beta}(h)\widetilde{\varrho}(h)}{p_*}\left[\partial_t h + \boldsymbol{u}\cdot\nabla h\right]. \tag{20a'}$$

Applying the method of characteristics to discretise the convection operators, the weak formulation reads

[11] We choose here a much smaller entrance velocity v_e to get a 3-phase flow.

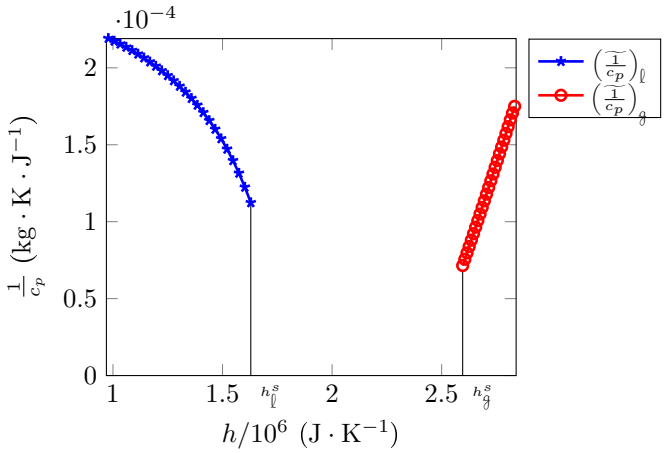

(a) Isobaric heat capacity.

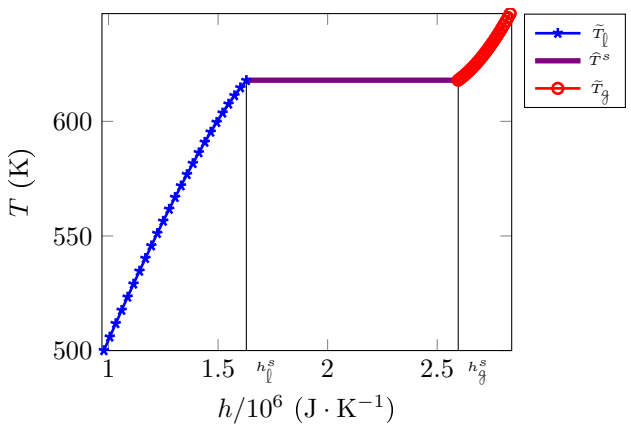

(b) Temperature.

Figure 6: Fitting polynomials for isobaric heat capacity (Table 7a) and temperature (Table 7b).

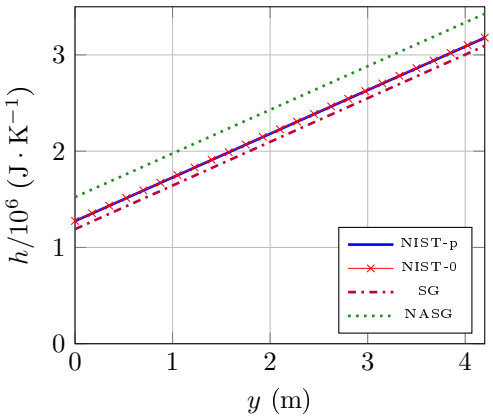

(a) Steady enthalpy

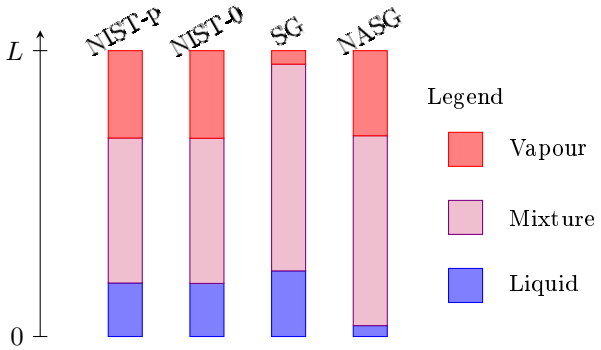

(b) Comparison of the phase distribution in the core

Figure 7: Steady solutions for different EOS

"**At time t^{n+1}, find $(\boldsymbol{u}^{n+1}, h^{n+1}, \mathcal{P}^{n+1}) \in (\boldsymbol{u}_e + \mathcal{U}) \times (h_e + \mathcal{H}) \times \mathrm{L}^2(\Omega^2)$ such that**

$$\iint_{\Omega^2} p_{\text{test}}\, \nabla\cdot \boldsymbol{u}^{n+1}\, \mathrm{d}\boldsymbol{x} = \iint_{\Omega^2} \frac{\widetilde{\beta}(h^n)\widetilde{\varrho}(h^n)}{p_*} \frac{h^{n+1} - h^n(\boldsymbol{\xi}^n)}{\Delta t} p_{\text{test}}\, \mathrm{d}\boldsymbol{x}, \qquad \forall\, p_{\text{test}} \in \mathrm{L}^2,$$

$$\iint_{\Omega^2} \widetilde{\varrho}(h^n) \frac{h^{n+1} - h^n(\boldsymbol{\xi}^n)}{\Delta t} h_{\text{test}}\, \mathrm{d}\boldsymbol{x} = \iint_{\Omega^2} \Phi(t^{n+1}, \cdot) h_{\text{test}}\, \mathrm{d}\boldsymbol{x} - \iint_{\Omega^2} \widetilde{\Lambda}(h^n) \nabla h^{n+1} \cdot \nabla h_{\text{test}}\, \mathrm{d}\boldsymbol{x}, \qquad \forall\, h_{\text{test}} \in \mathcal{H},$$

$$\iint_{\Omega^2} \widetilde{\varrho}(h^n) \frac{\boldsymbol{u}^{n+1} - \boldsymbol{u}^n(\boldsymbol{\xi}^n)}{\Delta t} \cdot \boldsymbol{u}_{\text{test}}\, \mathrm{d}\boldsymbol{x} + \iint_{\Omega^2} \frac{\widetilde{\mu}(h^n)}{2} \left(\nabla \boldsymbol{u}^{n+1} + (\nabla \boldsymbol{u}^{n+1})^T\right) :: \left(\nabla \boldsymbol{u}_{\text{test}} + \nabla \boldsymbol{u}_{\text{test}}^T\right)\, \mathrm{d}\boldsymbol{x}$$
$$+ \iint_{\Omega^2} \widetilde{\eta}(h^n)\, (\nabla\cdot \boldsymbol{u}^{n+1})(\nabla\cdot \boldsymbol{u}_{\text{test}})\, \mathrm{d}\boldsymbol{x} - \iint_{\Omega^2} \mathcal{P}^{n+1}\, \nabla\cdot \boldsymbol{u}_{\text{test}}\, \mathrm{d}\boldsymbol{x} = \iint_{\Omega^2} \widetilde{\varrho}(h^n) \boldsymbol{g} \cdot \boldsymbol{u}_{\text{test}}\, \mathrm{d}\boldsymbol{x}, \qquad \forall\, \boldsymbol{u}_{\text{test}} \in \mathcal{U},"$$

where

$$\mathcal{H} = \left\{\theta \in \mathrm{H}^1(\Omega^2) \colon \theta(x,0) = 0\right\},$$
$$\mathcal{U} = \left\{\boldsymbol{v} \in \left(\mathrm{H}^1(\Omega^2)\right)^2 \colon \boldsymbol{v}(x,0) = \boldsymbol{0},\ \boldsymbol{v}\cdot\boldsymbol{n}(0,y) = \boldsymbol{v}\cdot\boldsymbol{n}(L_x,y) = 0\right\},$$

and $\boldsymbol{\xi}^n$ is a numerical approximation of $\boldsymbol{\xi}(t^n; t^{n+1}, \boldsymbol{x})$ where $\boldsymbol{\xi}$ is the solution of the characteristic equation:

$$\begin{cases} \dfrac{\mathrm{d}\boldsymbol{\chi}}{\mathrm{d}\tau} = \boldsymbol{u}\big(\tau, \boldsymbol{\chi}(\tau; t, \boldsymbol{x})\big), \\[2ex] \boldsymbol{\chi}(t; t, \boldsymbol{x}) = \boldsymbol{x}. \end{cases}$$

Notice that due to discontinuities of most coefficients across (potential) level sets Γ_ℓ and Γ_ϑ, there should be some interface terms in the weak formulation, but they vanish due to jump conditions (21). In particular, there is no need to track the interfaces, which reduces the computational costs.

We do not give more details either about the mathematical content or the numerical treatment, since the problem is simulated by means of `FreeFem++` [57], which solves directly the weak formulation given above.

We recall that the parameters $\widetilde{\beta}$ and $\widetilde{\varrho}$ are given in Table 6.

Remark 5.1. *The substitution of Equation* (20a) *by* (20a') *makes the weak formulation easier to solve. Equation* (20a) *would lead to*

$$\iint_{\Omega^2} p_{test}\, \nabla\cdot \boldsymbol{u}^{n+1}\, \mathrm{d}\boldsymbol{x} = \iint_{\Omega^2} \frac{\beta(h^n) p_{test}}{p_*} \Phi\, \mathrm{d}\boldsymbol{x} - \iint_{\Omega^2} \Lambda(h^n, p_*) \nabla h^{n+1} \cdot \left[\frac{\partial \beta}{\partial h}(h^n, p_*) \frac{p_{test}}{p_*} \nabla h^n + \frac{\beta(h^n)}{p_*} \nabla p_{test}\right] \mathrm{d}\boldsymbol{x}.$$

This would require to increase the regularity of p_{test} and to approximate the function $\frac{\partial \beta}{\partial h}$, which may induce instabilities. Replacing the right hand side in (20a) *by the left hand side in* (20b) *enables to overcome all these issues.*

5.2 Data

Choice of the equation of state First, let us observe that a first comparison between the Stiffened Gas law, the Noble-Abel Stiffened Gas one, and the two different tabulated approaches (NIST-p and NIST-0) has been done in Section 4.3, since the differences can already be observed on the steady states in 1D. Further comparisons in 2D are performed in § 5.4.2.

Physical and numerical parameters Based on the numerical scheme detailed above, we perform some simulations with our tabulated EOS, aiming at:

1. verifying our code by means of comparisons with explicit steady solutions inferred from dimension 1 (see § 5.3);
2. highlighting the accuracy of the tabulated approach to describe the physics of water in a PWR (see § 5.4.2);
3. showing the low influence of thermal conduction for physically relevant data in a PWR (see § 5.4.3);
4. showing the ability of the model and of the 2D scheme to capture the flow complexity by emphasizing the influence of the gravity orientation (see § 5.4.4).

Parameters are set as follows to simulate a PWR:

- Geometry: $L_x = 1\,\mathrm{m}$, $L_y = 2\,\mathrm{m}$.
- Discretisation parameters: 40 nodes on the horizontal boundaries, 80 nodes on the vertical boundaries, which results in an unstructured mesh generated by `FreeFem++` with 3740 vertices and a characteristic length h of the mesh around 2 cm. The mesh can be seen on Figures 9.
- Reference values: $p_* = 15.5\,\mathrm{MPa}$, $\Phi_\star = 170 \times 10^6\,\mathrm{W}\cdot\mathrm{m}^{-3}$, $\varrho_e = 750\,\mathrm{kg}\cdot\mathrm{m}^{-3}$, $D_e = 375\,\mathrm{kg}\cdot\mathrm{m}^{-2}\cdot\mathrm{s}^{-1}$.
- Initial data: $h^0(x,y) = \varrho^{-1}(\varrho_e)$, $\boldsymbol{u}^0(x,y) = (u^0(x,y), v^0(x,y)) = (0, D_e/\varrho_e)$.
- The power density Φ (constant or not) is specified in each section.
- The use of the method of characteristics makes the numerical schemes unconditionally stable. Consequently, there is no constraint upon the time step. But to ensure a good accuracy, we cannot let the time step be too large. We set $\Delta t = 0.01\,\mathrm{s} \sim \frac{h}{v_e}$.

In every test case, we check that the Mach number remains small in all phases during the whole computation, in order to ensure the validity of our low Mach number model. The Mach number is computed from the speed of sound, with NIST-p tabulated values for pure phases, and Formula (29) given in Appendix C for the mixture.

5.3 Validation of the 2D numerical scheme

In this test case, we aim at validating our two-dimensional numerical scheme. To this end, we chose the power density $\Phi(x,y)$ to be uniformly constant equal to $2\Phi_\star$, which produces a quasi 1D case. Starting from a domain initially filled with liquid, this leads to the appearance of both mixture and vapour. The computation is performed with the NIST-p data given in Table 2.In order to compare with the predicted asymptotic solution given in Proposition 4.1, we neglect thermal conductivity for this test case. Thus, the steady solution for the enthalpy in 1D is given by

$$h(y) = \widetilde{\varrho}^{-1}(\varrho_e) + \frac{2\Phi_\star}{D_e} y \simeq 1.273 \times 10^6 + 1.36 \times 10^6 y.$$

In our computation, we observe a numerical convergence towards an asymptotic solution. The relative difference between this asymptotic solution and the 1D steady solution is of order 10^{-2}, and reaches a maximum value of 1% at the top of the domain. This shows the good matching between the two solutions.

Moreover, we observe that this 2D computation on unstructured mesh allows to capture a 2D solution independent of the variable x, as shown on Figure 8.

5.4 Phase transition with a compactly supported heating

In all the test cases of this section, the power density is chosen to be compactly supported within a disc in the lower part of the core, which yields a genuine 2D case:

$$\Phi(x,y) = 20\Phi_\star \mathbf{1}_{\{(x-0.5)^2+(y-0.5)^2 \leqslant 0.125^2\}}(x,y).$$

We can see on Figure 9(a) the location of the power density (where the fluid is heated).

5.4.1 Reference test case

The values given in § 5.2 with $\lambda \equiv 0$ lead to a scenario in which the temperature increases as the flow passes through the heat source and some mixture appears as seen on Figure 10(a). The NIST-p approach described in § 3.1.2 is used for the equation of state. The mixture phase has a lower density than the liquid phase. Hence, as the flows goes upwards and the gravity field is pointing downwards, a Rayleigh-Taylor instability occurs (see Figure 9(b)): the gravity makes the lighter phase speed up through the heavier phase above (Archimedes' principle). The instability is well recovered by the numerical scheme over this mesh.

In addition, we plot the Mach number of the flow at time $t = 0.55\,\mathrm{s}$ on Figure 10(d), which is the time for which the flow is the most mixed up. We notice that it remains small (of order 10^{-2} at the maximum), which guarantees the validity of our low Mach number model for such flows. It is in particular the case in the mixture phase where the speed of sound is decreasing. The temperature and the norm of the velocity are also plotted at the same time on Figure 10. The location of mixture in the flow is in particular observed on Figure 10(c), where the temperature is constant and equal to $\widehat{T}^s = 617.939\,\mathrm{K}$.

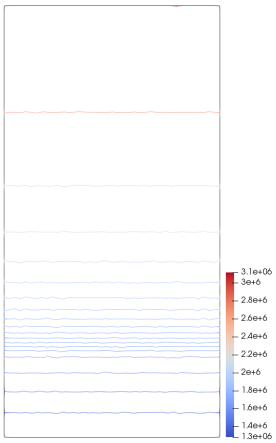

Figure 8: Isolines of enthalpy at time $t = 1.6\,\mathrm{s}$ (asymptotic state) (test case of § 5.3)

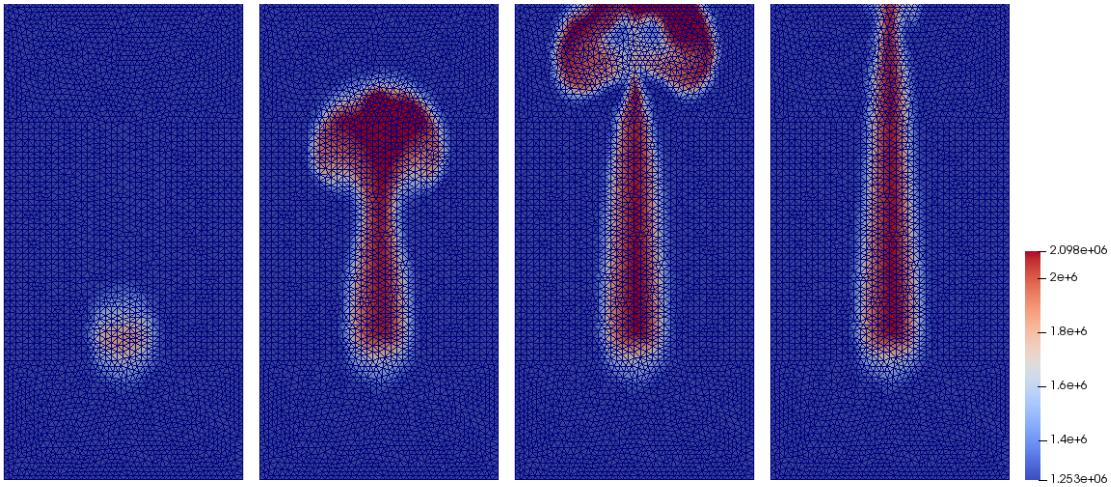

(a) $t = 0.10\,\mathrm{s}$ (b) $t = 0.40\,\mathrm{s}$ (c) $t = 0.55\,\mathrm{s}$ (d) $t = 0.80\,\mathrm{s}$

Figure 9: Enthalpy for a 2D flow with phase transition at different times (test case of § 5.4.1, EOS : NIST-p)

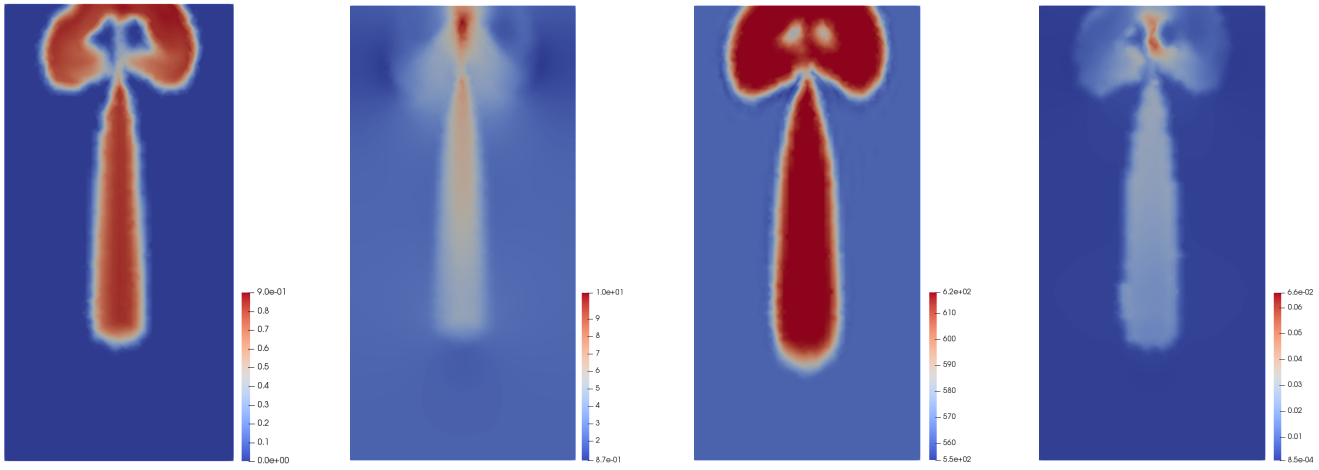

(a) Volume fraction (b) Magnitude of the velocity (c) Temperature (d) Mach number

Figure 10: Density, velocity, temperature and Mach number at time $t = 0.55\,\mathrm{s}$ (test case of § 5.4.1, EOS : NIST-p)

5.4.2 Influence of the EOS

In this section, we observe the discrepancy induced by the use of different EOS in a 2D unsteady test case. In practical terms, we compare the strategies we introduced in Section 3, namely ❶-❷ for the SG/NASG EOS, ❸ for high-order polynomial-fitting and ❹ for constant approximations.

We observe on Figure 11 that NIST-p and NIST-0 approaches lead to very similar results, whereas the SG EOS induces a largely over-estimated temperature. The NASG EOS is not presented here, since we already observed on Figure 7(a) that it overestimates the entrance enthalpy h_e computed from ϱ_e, and it thus leads here to very different results, with a much higher temperature. We recover the fact that for such accidental situations, academic EOS like SG/NASG are not appropriate.

5.4.3 Influence of the thermal conductivity

In this test case, the influence of thermal conductivity is investigated. The computations are performed with the NIST-p data given in Tables 2 and 7.

The order of magnitude of the thermal conductivity is given in Table 1 (around 10^{-1}). We observe on Figure 12 the difference between numerical solutions with and without thermal diffusion at time 0.55 s. The error is of order 10^{-4}, which shows that for the physical situations we are interested in, the thermal conductivity does not play a major role.

5.4.4 Influence of the gravity field

Since our choice of 2D power density generates hydrodynamic instabilities apparently driven by gravity effects, we focus on the impact of the gravity field direction. Again, the computations are performed with the NIST-p data given in Tables 2 and 7.

Figure 13 depicts the same test case as in § 5.4.3 except for the gravity field whose orientation varies (downwards/null/upwards/to the right).

In the classic situation where the gravity is oriented downwards (Figure 13(a)), the flow driven by the material velocity is sped up by the gravity effects which makes the mixture phase (which is lighter than the liquid phase) go upwards (see § 5.4.3 for more details about the appearance of the Rayleigh-Taylor instability). Without gravity (Figure 13(b)), there is a unique physical phenomenon (forced convection) that governs the motion of fluid. This explains that at the same time of evolution, the mixture cloud is lower than in the previous case (but hotter as the fluid remained longer within the core) and no Rayleigh-Taylor instability occurs. If the gravity field is upward (Figure 13(c)), there is a balance between the two aforementioned phenomena. The flow velocity makes the mixture go to the top while the gravity makes it go to the bottom, as it is lighter compared to the pure liquid phase. The motion is even slower than without gravity. As for the horizontal case (Figure 13(d)), we observe that the mixture tends to the left which is the opposite direction to the gravity field, as expected. Hence, we see that our numerical scheme enables to catch various types of behaviour depending on the data.

Conclusion & Perspectives

The ultimate strategy to simulate a fluid flow in a nuclear core would rely on ① a compressible model coupled to a tabulated equation of state satisfying thermodynamic laws and accounting for phase transition and on ② an accurate and robust numerical scheme able to treat any Mach regime with a "reasonable" computational cost. In our opinion, this seems currently out of reach. That is why we propose in this paper a compromise between accuracy and efficiency by focusing on a specific regime – namely the low Mach number regime – by means of a reduced-complexity model which turns out to be physically relevant [58]: the hypothesis of a small Mach number indeed holds in nominal regime.

The low Mach number model under study (Lmnc) is supplemented with an original construction of an incomplete equation of state dedicated to constant thermodynamic pressure states. It relies on a polynomial-fitting procedure whose degree can be chosen by the user. This leads to a natural numerical scheme which is easy to implement, which satisfies basic thermodynamic requirements and which leads to a much smaller computational cost than it would be with a compressible model coupled to a tabulated law like IAPWS [40–42]. The overall method is assessed by means of analytical and stiff test cases involving phase transition, where classic analytical EOS fail to provide relevant values.

We investigated two cases for the degree of fitting polynomials: NIST-p (high-order) and NIST-0 (low-order). Theoretical (§ 4.3) and numerical (§ 5.4.2) results tend to show that the choice of the degree does not have a significant impact on the accuracy. On the contrary, comparisons between NIST-0 and the *Stiffened Gas* law (for which the density has a similar algebraic expression) prove that the crucial point is to exactly satisfy saturation points. The

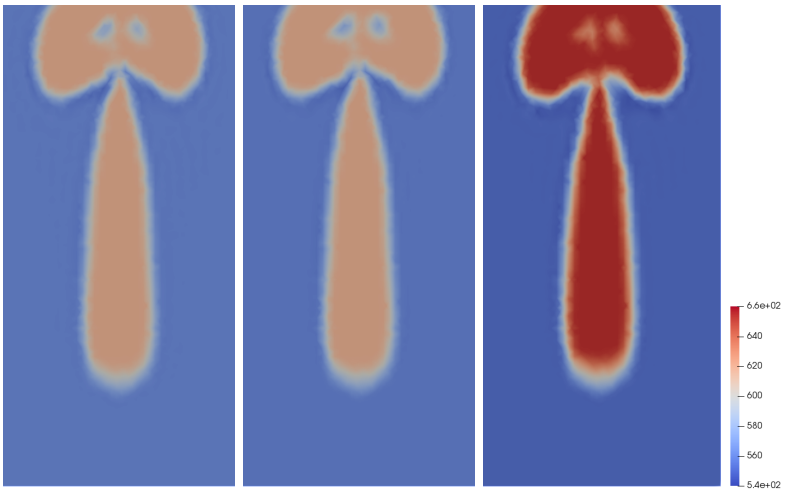

(a) ❸ for NIST-p (b) ❹ for NIST-0 (c) ❶ for the SG EOS

Figure 11: Temperature at time $t = 0.55\,\mathrm{s}$ with different EOS (test case of § 5.4.2)

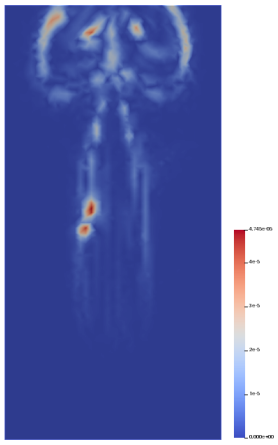

Figure 12: Relative difference between numerical enthalpies with $\lambda = 0$ and $\lambda \neq 0$ at time $t = 0.55\,\mathrm{s}$ (test case of § 5.4.3, EOS : NIST-p)

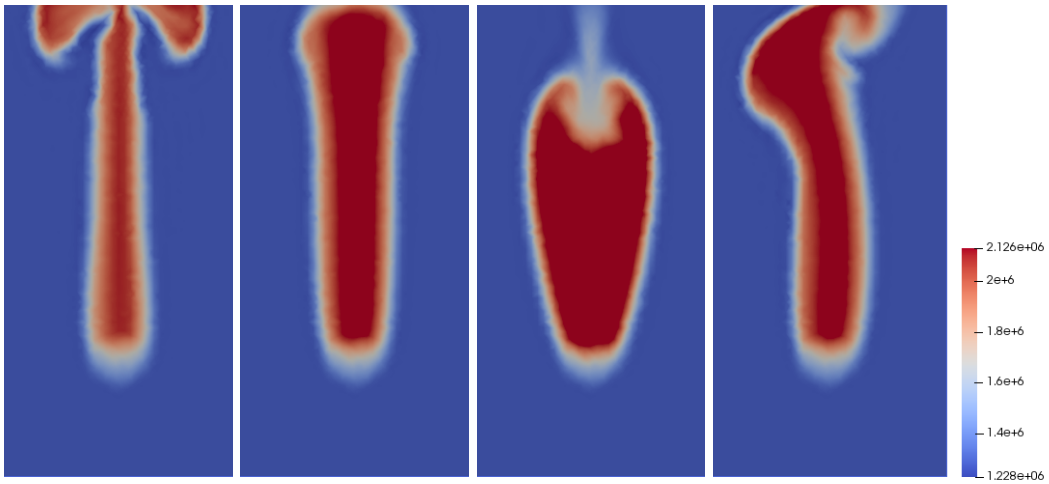

(a) $\boldsymbol{g} = (0, -g)$ (b) $\boldsymbol{g} = (0, 0)$ (c) $\boldsymbol{g} = (0, g)$ (d) $\boldsymbol{g} = (g, 0)$

Figure 13: Enthalpy at time 0.55 s for several orientations of the gravity field (test case of § 5.4.4)

discrepancy between h_κ^s deduced from the SG law and $\widehat{h}_\kappa^s$ used in our strategy induces quite different results as presented in § 5.4.2. We mention that the procedure described in this paper can be adapted by end-users (numerical method to fit polynomials, range of temperatures, pressure value, ...) depending on the applications.

Previous papers on the Lmnc model were based on the SG law in order to develop and assess the numerical strategy. The present results henceforth enable to treat more realistic applications and to provide reliable forecasts in incidental situations. Future works will deal with more general equilibria implying a hierarchy of n-equation models (see for instance [59, 60]).

A Stiffened Gas (SG) and Noble-Abel – Stiffened Gas (NASG) equations of state

Let us give some details about the complete equation of state (6). Parameters $\overline{c}_v$, $\overline{\gamma}$, $\overline{\pi}$, $\overline{b}$, $\overline{Q}$ and $\overline{\mathcal{S}}_0$ are constants describing thermodynamic properties of the fluid: $\overline{c}_v > 0$ is the isochoric heat capacity, $\overline{\gamma} = \frac{\overline{c}_p}{\overline{c}_v} > 1$ the ratio of isobaric and isochoric heat capacities[12], $\overline{\pi} \geq 0$, $\overline{b} > 0$ is the co-volume, $\overline{Q}$ the binding energy and $\overline{\mathcal{S}}_0$ a reference entropy. The latter parameter may often be replaced by the following one

$$\overline{Q}' \stackrel{\text{def}}{=} \overline{\mathcal{S}}_0 + \overline{c}_v \left[\overline{\gamma} \ln(\overline{c}_v) + (\overline{\gamma} - 1) \ln(\overline{\gamma} - 1)\right].$$

The domain of definition of $\mathcal{S}$ is the set $\tau > \overline{b}$ and $\varepsilon - \overline{Q} - \overline{\pi}(\tau - \overline{b}) > 0$. The parameters used in this law describing a pure phase are determined by using a reference curve, usually in the (τ, p)-plane. For example, values for water and steam computed in [37] for SG and in [38] for NASG are given in Table 8. These values yield reasonable approximations over a range of temperature from 300 K to 500 K.

Using the fundamental thermodynamic relation $T\mathrm{d}\mathcal{S} = \mathrm{d}\varepsilon + p\mathrm{d}\tau$ and introducing classic potentials, we have

$$(\tau, \varepsilon) \mapsto T(\tau, \varepsilon) = \frac{1}{\frac{\partial \mathcal{S}}{\partial \varepsilon}\big|_\tau} = \frac{\varepsilon - \overline{Q} - \overline{\pi}(\tau - \overline{b})}{\overline{c}_v}, \qquad \text{[temperature]}$$

$$(\tau, \varepsilon) \mapsto p(\tau, \varepsilon) = T \left.\frac{\partial \mathcal{S}}{\partial \tau}\right|_\varepsilon = (\overline{\gamma} - 1)\frac{\varepsilon - \overline{Q}}{\tau - \overline{b}} - \overline{\gamma}\overline{\pi}, \qquad \text{[pressure]}$$

$$(\tau, \varepsilon) \mapsto h(\tau, \varepsilon) = \varepsilon + p\tau = \varepsilon + \tau\left[(\overline{\gamma} - 1)\frac{\varepsilon - \overline{Q}}{\tau - \overline{b}} - \overline{\gamma}\overline{\pi}\right], \qquad \text{[enthalpy]}$$

$$\begin{aligned}(\tau, \varepsilon) \mapsto c^2(\tau, \varepsilon) &\stackrel{\text{def}}{=} \left.\frac{\partial p}{\partial \varrho}\right|_s = -\frac{\tau^2}{T}\left(\left.\frac{\partial^2 \mathcal{S}}{\partial \tau^2}\right|_\varepsilon - 2p\frac{\partial^2 \mathcal{S}}{\partial \tau \partial \varepsilon} + p^2 \left.\frac{\partial^2 \mathcal{S}}{\partial \varepsilon^2}\right|_\tau\right) \\ &= \overline{\gamma}(\overline{\gamma} - 1)\left(\varepsilon - \overline{Q} - \overline{\pi}(\tau - \overline{b})\right)\frac{\tau^2}{(\tau - \overline{b})^2}. \qquad \text{[speed of sound]}\end{aligned}$$

Set $\widehat{Q}(p) \stackrel{\text{def}}{=} \overline{Q} + \overline{b}p$. Thus, by inverting the function $(\tau, \varepsilon) \mapsto (h, p)$

$$(h, p) \mapsto \tau(h, p) = \frac{\overline{\gamma} - 1}{\overline{\gamma}}\frac{h - \widehat{Q}(p)}{p + \overline{\pi}} + \overline{b}, \qquad \text{[volume]}$$

$$(h, p) \mapsto \beta(h, p) \stackrel{\text{def}}{=} p \left.\frac{\partial \tau}{\partial h}\right|_p = \frac{\overline{\gamma} - 1}{\overline{\gamma}}\frac{p}{p + \overline{\pi}}, \qquad \text{[compressibility coefficient]}$$

$$(h, p) \mapsto q(h, p) \stackrel{\text{def}}{=} \widehat{Q}(p) - \frac{p}{\beta(h, p)}\overline{b},$$

$$(h, p) \mapsto \varrho(h, p) = \frac{1}{\tau(h, p)} = \frac{p/\beta(h, p)}{h - q(h, p)}, \qquad \text{[density]}$$

$$(h, p) \mapsto T(h, p) = \frac{h - \widehat{Q}(p)}{\overline{\gamma}\overline{c}_v}. \qquad \text{[temperature]}$$

The case of a stiffened gas law is recovered by setting $\overline{b} = 0$ (so that $q = \widehat{Q} = \overline{Q}$). The case of a perfect gas law is recovered by setting $\overline{b} = \overline{Q} = \overline{\pi} = 0$.

[12] Adopting the same convention as in [36, 61], the polytropic coefficient or adiabatic exponent γ is defined by $\gamma(\tau, \mathcal{S}) \stackrel{\text{def}}{=} -\frac{\tau}{P}\left.\frac{\partial P}{\partial \tau}\right|_{\mathcal{S}}$. Except in the case of polytropic gases, this coefficient differs from the widely used ratio of heat capacities. For the NASG EOS, γ is related to the ratio of heat capacities by the relation $\gamma = (1 + \frac{\pi}{p})\overline{\gamma}$.

Phase	$\overline{c_v}$ [J · K^{-1}]	$\overline{\gamma}$	$\overline{\pi}$ [Pa]	$\overline{Q}$ [J · kg^{-1}]	$\overline{b}$ [m^3 · kg^{-1}]	$\overline{Q}'$ [J · kg^{-1}]
Liquid NASG	3202	1.39	8899×10^5	-1244.191×10^3	4.78×10^{-4}	0
Steam NASG	462	1.95	0	2287.484×10^3	0	6417
Liquid SG	1816.2	2.35	10^9	-1167.056×10^3	0	0
Steam SG	1040.14	1.43	0	2030.255×10^3	0	−23 310

Table 8: Water and steam. Values for NASG laws from [38]. Values for SG laws from [37].

B Expressions of the compressibility coefficient β

We note $\tau \overset{\text{def}}{=} 1/\varrho$, so that $\beta = p \left.\dfrac{\partial \tau}{\partial h}\right|_p$. We recall the following classic definitions:

$$(c^*)^2(\tau, \mathcal{S}) \overset{\text{def}}{=} -\tau^2 \left.\frac{\partial p}{\partial \tau}\right|_{\mathcal{S}}, \qquad c_v \overset{\text{def}}{=} T \left.\frac{\partial \mathcal{S}}{\partial T}\right|_{\tau}, \qquad c_p \overset{\text{def}}{=} T \left.\frac{\partial \mathcal{S}}{\partial T}\right|_{p}, \tag{23}$$

where $\mathcal{S}$ is the specific entropy. We first remark that[13]

$$\frac{c_p}{c_v} = \frac{T \left.\frac{\partial \mathcal{S}}{\partial T}\right|_p}{T \left.\frac{\partial \mathcal{S}}{\partial T}\right|_\tau} = \frac{-\left.\frac{\partial T}{\partial \tau}\right|_{\mathcal{S}} \left.\frac{\partial \tau}{\partial \mathcal{S}}\right|_T}{-\left.\frac{\partial p}{\partial \mathcal{S}}\right|_T \left.\frac{\partial T}{\partial p}\right|_{\mathcal{S}}} = \left.\frac{\partial p}{\partial \tau}\right|_{\mathcal{S}} \left.\frac{\partial \tau}{\partial p}\right|_T = -\frac{(c^*)^2}{\tau^2} \left.\frac{\partial \tau}{\partial p}\right|_T. \tag{24}$$

Then

$$c_p - c_v = T\left(\left.\frac{\partial \mathcal{S}}{\partial T}\right|_p - \left.\frac{\partial \mathcal{S}}{\partial T}\right|_\tau\right) = T\left(\left.\frac{\partial \mathcal{S}}{\partial T}\right|_\tau + \left.\frac{\partial \mathcal{S}}{\partial \tau}\right|_T \left.\frac{\partial \tau}{\partial T}\right|_p - \left.\frac{\partial \mathcal{S}}{\partial T}\right|_\tau\right) = T \left.\frac{\partial \mathcal{S}}{\partial \tau}\right|_T \left.\frac{\partial \tau}{\partial T}\right|_p = T \left.\frac{\partial p}{\partial T}\right|_\tau \left.\frac{\partial \tau}{\partial T}\right|_p$$

due to the Maxwell relation associated to the free energy $\mathcal{F}$ that satisfies $\mathrm{d}\mathcal{F} = -p\mathrm{d}\tau - \mathcal{S}\mathrm{d}T$. Hence

$$c_p - c_v = -T \frac{\left.\frac{\partial \tau}{\partial T}\right|_p}{\left.\frac{\partial T}{\partial \tau}\right|_p \left.\frac{\partial \tau}{\partial p}\right|_T} \overset{(24)}{=} T \frac{c_v}{c_p} \frac{(c^*)^2}{\tau^2} \left(\left.\frac{\partial \tau}{\partial T}\right|_p\right)^2. \tag{25}$$

Since the enthalpy satisfies the principle $\mathrm{d}h = T\mathrm{d}\mathcal{S} + \tau \mathrm{d}p$, then $T \left.\frac{\partial \mathcal{S}}{\partial T}\right|_p = \left.\frac{\partial h}{\partial T}\right|_p$ so that

$$\frac{1}{c_p} = \left.\frac{\partial T}{\partial h}\right|_p. \tag{26}$$

Finally

$$\beta = p \left.\frac{\partial \tau}{\partial h}\right|_p = p \left.\frac{\partial \tau}{\partial T}\right|_p \left.\frac{\partial T}{\partial h}\right|_p \overset{(26)}{=} \frac{p}{c_p} \left.\frac{\partial \tau}{\partial T}\right|_p \overset{(25)}{=} \frac{p\tau}{c^* \sqrt{T}} \sqrt{\frac{1}{c_v} - \frac{1}{c_p}},$$

which proves (8).

Further, we can compute

$$\left.\frac{\partial T}{\partial P}\right|_h = -\frac{\left.\frac{\partial h}{\partial P}\right|_T}{\left.\frac{\partial h}{\partial T}\right|_P} = -\frac{\left.\frac{\partial h}{\partial P}\right|_T}{c_p} = -\frac{\tau - T \left.\frac{\partial \tau}{\partial T}\right|_P}{c_p} = -\frac{\tau}{c_p} + \frac{T}{P}\beta, \tag{27}$$

where $\left.\dfrac{\partial T}{\partial P}\right|_h$ is the Joule-Thomson coefficient. Expression (9) immediately follows.

[13] We make use of the following formula: for an EOS $f(X_1, X_2, X_3) = 0$, we have $\left.\frac{\partial X_1}{\partial X_2}\right|_{X_3} \left.\frac{\partial X_2}{\partial X_3}\right|_{X_1} \left.\frac{\partial X_3}{\partial X_1}\right|_{X_2} = -1$.

p [MPa]	ρ_l^s [kg m^{-3}]	h_l^s [kJ kg^{-1}]	ρ_g^s [kg m^{-3}]	h_g^s [kJ kg^{-1}]
$p_{-1} = 15{:}499$	594.397161363	1629.84051905	101.919399943	2596.14861770
$p_0 = 15{:}500$	594.378648626	1629.87998125	101.930084802	2596.11873446
$p_1 = 15{:}501$	594.360134886	1629.91944396	101.940770824	2596.08884821

Table 9: Data on saturation curve to compute $(\rho_l^s)'$, $(\rho_g^s)'$, $(h_l^s)'$ and $(h_g^s)'$ depending on p. Values for water [39]

C Mach number and speed of sound of the two-phase flow

To evaluate the Mach number in the diffential system and verify that it remains low, we need to compute the speed of sound. It is given by

$$c(h;p) \overset{\text{def}}{=} \sqrt{\frac{\partial p}{\partial \rho}_s} = \sqrt{\frac{1}{\frac{1}{\rho(h;p)}\frac{\partial \rho}{\partial h}(h;p) + \frac{\partial \rho}{\partial p}(h;p)}} = \begin{cases} c_l(h;p), & \text{if } h \leq h_l^s, \\ c_m(h;p), & \text{if } h_l^s < h < h_g^s, \\ c_g(h;p), & \text{if } h \geq h_g^s. \end{cases} \tag{28}$$

In pure phases, we can fit the speed of sound with a polynomial based on the NIST table [39] as previously, but for the sake of consistency, we choose to match the new expression (8) of which provides a fitting function (which is no more a polynomial). For instance, with a NIST-p strategy for both c and c_p, the relative error between this construction and the values extracted from the tables are $6{:}85 \cdot 10^{-3}$ in the liquid phase and $5{:}64 \cdot 10^{-3}$ in the vapour phase.

In the mixture, the speed of sound at mechanic and thermodynamic equilibrium is given by (see [2] for details)

$$\frac{1}{c_m}^2(h;p) = \frac{[\chi(h;p)(\rho_g)'(p) + (1-\chi(h;p))(\rho_l)'(p)]q_m(p) + \chi(h;p)(\rho_g h_g^s)'(p) + (1-\chi(h;p))(\rho_l h_l^s)'(p) - 1}{h - q_m(p)}. \tag{29}$$

where $(\rho^s)'$ and $(\rho h^s)'$ are the derivatives of $p \mapsto \rho^s(p)$ and $p \mapsto \rho^s(p)h^s(p)$. When one uses analytical EOS in pure phases, we can differentiate these relations to obtain those derivatives (as in [2] with the SG law). In the present case, as we use tabulated values in pure phases, $(\rho^s)'$ and $(h^s)'$ are approximated by centered finite differences:

$$(\rho^s)'(p_{-1}) = \frac{\rho^s(p_{-1}) - \rho^s(p_1)}{p_{-1} - p_1}; \qquad (\rho^s h^s)'(p_{-1}) = \frac{\rho^s(p_{-1})h^s(p_{-1}) - \rho^s(p_1)h^s(p_1)}{p_{-1} - p_1};$$

where p_i, $\rho^s(p_i)$ and $h^s(p_i)$, $i = -1; 0; 1$, are obtained from experimental data (see Table 9 for the pressure of interest $p = 15{:}5$ MPa).

Note that $c_m\big(h^s(p);p\big) < c\big(h^s(p);p\big)$, see for example [36, 54].

Remark C.1. In [52, 62], another equivalent expression is used:

$$\frac{1}{c_m}^2(h;p) = \rho_m(h;p)\left(\frac{\chi(h;p)}{\rho_g(p)(c_g^s)^2(p)} + \frac{1-\chi(h;p)}{\rho_l(p)(c_l^s)^2(p)} + T^s(p)\left(\chi(h;p)\rho_g'(p)\,{}_gc_{v_g}{}^2{}_g(p) + (1-\chi(h;p))\rho_l'(p)\,{}_lc_{v_l}{}^2{}_l(p)\right)\right)$$

where $\chi(h;p) = \frac{\rho(h;p)-\rho_m(p)}{\rho}$ and $(c^s)(p) = c\big(h^s(p);p\big)$ is the speed of sound of the pure phase at saturation.

References

[1] A. Bondesan, S. Dellacherie, H. Hivert, J. Jung, V. Lleras, C. Mietka, Y. Penel, Study of a depressurisation process at low Mach number in a nuclear core reactor, in: CEMRACS 2015: Coupling multi-physics models involving fluids, Vol. 55 of ESAIM: ProcS, 2015, pp. 41–60.

[2] M. Bernard, S. Dellacherie, G. Faccanoni, B. Grec, Y. Penel, Study of a low Mach nuclear core model for two-phase flows with phase transition I: stiffened gas law, ESAIM Math. Model. Numer. Anal. 48 (6) (2014) 1639–1679.

[3] S. Dellacherie, On a low Mach nuclear core model, in: SMAI 2011, Vol. 35 of ESAIM:Proc, 2012, pp. 79–106.

[4] S. Dellacherie, G. Faccanoni, B. Grec, E. Nayir, Y. Penel, 2D numerical simulation of a low Mach nuclear core model with stiffened gas using FreeFem++, in: SMAI 2013, Vol. 45 of ESAIM:ProcS, 2014, pp. 138–147.